A Signal Simulation Framework for the CBM-TRD FEE

Master's Thesis in Physics

Institut für Kernphysik
WWU Münster

Hannes Morgenweck

supervised by

Anton Andronic

and

Christian Klein-Bösing

August 28, 2023

First referee: Prof. Dr. Anton Andronic

Second referee: Apl. Prof. Dr. Christian Klein-Bösing

Contents

1 Introduction

With worldwide effort and technical progress, mankind was able to observe and study smaller and smaller phenomena. This is especially true in the field of physics. The next big hurdle is the understanding of the Quark Gluon Plasma (QGP), which describes a state at high temperatures or densities in which the quarks and gluons interact as quasi-free particles. One of the facilities to investigate the *Quantum Chromodynamics* (QCD) phase diagram and the transition to the QGP is the Facility for Antiproton and Ion Research (FAIR), which is currently under construction at the *GSI Helmholtzzentrum für Schwerionenforschung* (GSI) in Darmstadt. Therefore the *Compressed Baryonic Matter* (CBM) experiment is set up, which is a fixed target experiment that operates at high interaction rates up to 10 Mhz. The whole set up will consist of multiple detectors with different properties, one of them being the Transition Radiation Detector (TRD). The TRDs main purpose is particle tracking and the identification of electrons and positrons with momenta with $p > \ 1.0 \, \frac{\mathrm{GeV}}{\mathrm{c}}$ [TDR18].
With experiments of this magnitude and complexity, it is relevant to have a profound understanding how the detector behaves under different circumstances. For this thesis a simulation framework was created to simulate the Multi Wire Proportional Chamber (MWPC) and the readout chain of the TRD. It was used to simulate three different types of uncertainties as well as four different methods to reconstruct the signal and compare them concerning effective energy and spatial resolution.

2 Theoretical Background

2.1 Interaction of Particles with Matter

It is essential to understand the theoretical aspect of how particles interact with matter as it is of direct relevance for the basic detector physics. This chapter will describe the different processes of energy deposition inside a detector for charged particles and for photons.

2.1.1 Heavy Charged Particles

Moderately relativistic charged heavy particles, that are more massive than electrons, have their mean rate of energy loss in the range of $0.1 \lesssim \beta\gamma \lesssim 1000$. Most of the interactions are effected by single inelastic collisions between the heavy charged particles and shell electrons. This results in ionization of atoms in the material. The mean rate of energy loss can be described by the Bethe-Bloch equation [Tan+18]:

$$\left\langle -\frac{dE}{dx} \right\rangle = K z^2 \frac{Z}{A} \frac{1}{\beta^2} \left[\frac{1}{2} \ln \frac{2 m_e c^2 \beta^2 \gamma^2 W_{max}}{I^2} - \beta^2 - \frac{\delta(\beta\gamma)}{2} \right]. \tag{2.1}$$

With the variables and values taken from [Tan+18]:

K:	coefficient $4\pi N_A r_e^2 m_e c^2 = 0.307\,075\ \frac{\mathrm{MeVcm}^2}{\mathrm{mol}}$		
z:	charge number of incident particle	Z:	atomic number of absorber
A:	atomic mass of absorber	$m_e c^2$:	electron mass $\times c^2$
I:	mean excitation energy	$\delta(\beta\gamma)$:	density effect correction
W_{max}:	maximum energy transfer to an electron in a single collision		

This equation has an accuracy of a few percent for intermediate-Z materials. Figure 2.1 shows a graphical visualization of the mean energy loss of positive muons in copper, with the intermediate part being labeled Bethe. This region is described by equation 2.1 for intermediate $\beta\gamma$ [Tan+18].

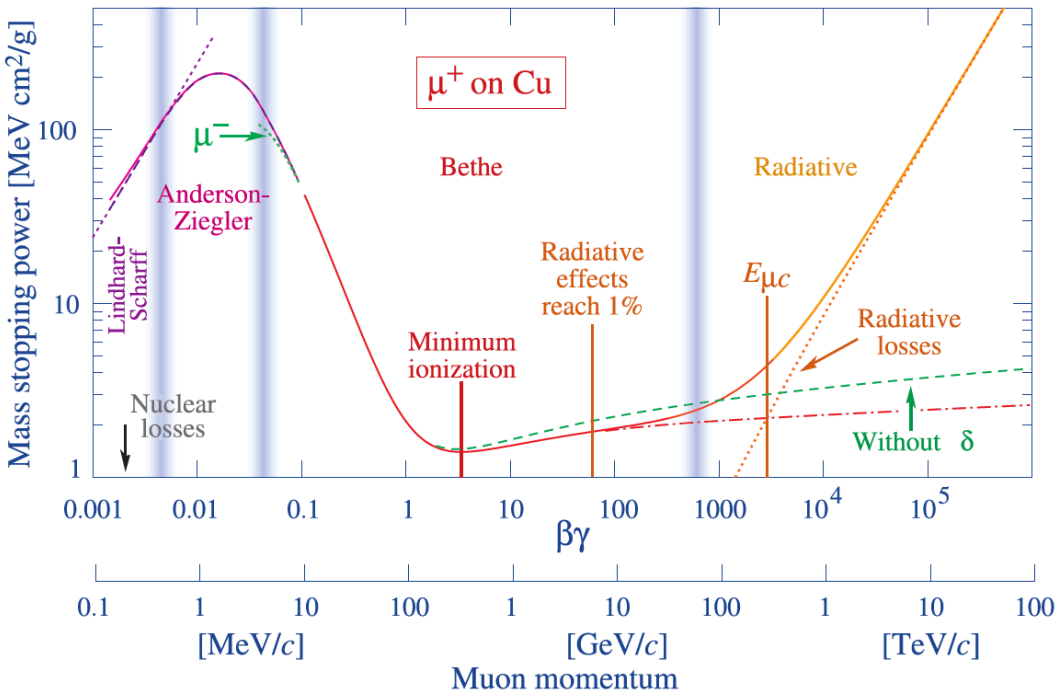

Figure 2.1: Mass stopping power $\langle -\mathrm{d}E/\mathrm{d}x \rangle$ (mean energy loss) of positive muons in copper depending on their $\beta\gamma$ [Tan+18].

2.1.2 Electrons

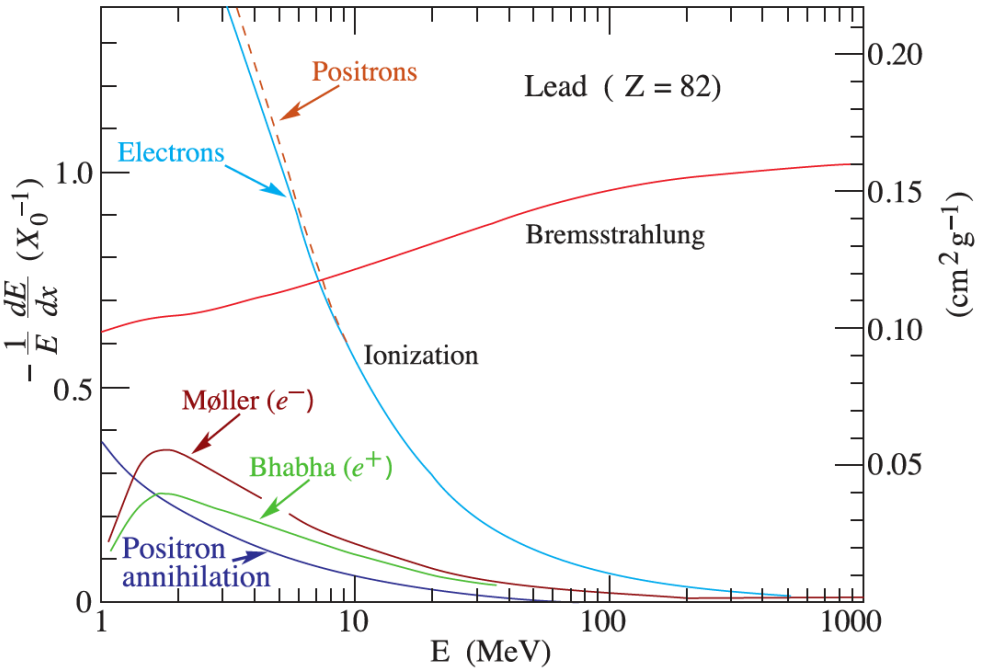

Figure 2.2: Fractional energy loss of electrons or positrons as a function of particle energy. The energy loss by collisions is dominant at lower energies, which rapidly decreases for increasing energy. At higher energies the dominant part is replaced by bremsstrahlung [Tan+18].

When electrons interact with matter they decelerate by ionizing, which is the dominant effect for lower energies (see Figure 2.2). On the other hand, bremsstrahlung becomes relevant at higher energies [Tan+18]. For the calculation of the energy loss of a particle by bremsstrahlung, the radiation length X_0, which is a material dependent parameter, is used.

$$\left(-\frac{dE}{dx}\right) = \frac{E}{X_0} \tag{2.2}$$

The radiation length X_0 describes the characteristic length a charged particle needs to travel until it loses $1 - \frac{1}{e} = 63\%$ of its initial energy by bremsstrahlung [Her16].

2.1.3 Photons

The interaction of photons with matter is different than the interaction of charged particles with matter. There are three types of interactions depending on the energy of the photon as shown in figure 2.3.

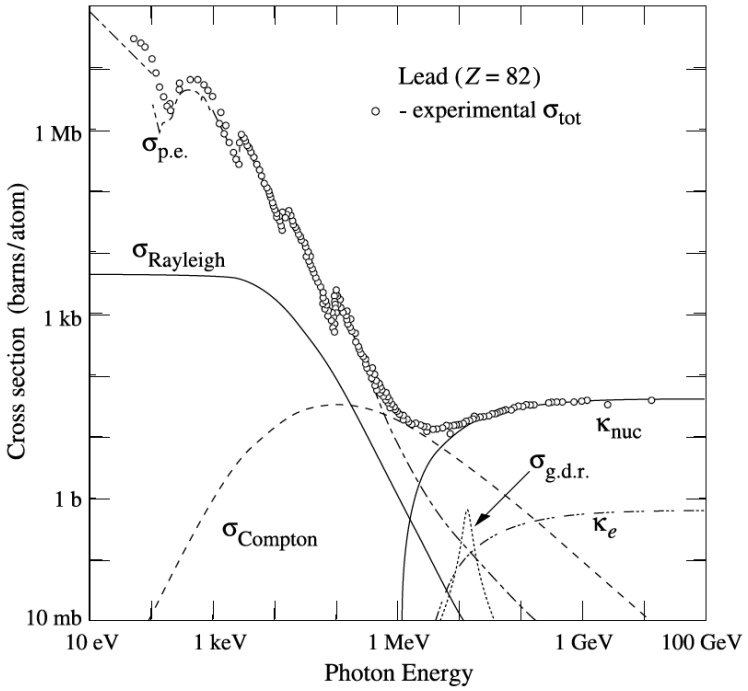

Figure 2.3: Total cross section for photons as a function of its energy in lead with different contributions [Her16](edited).

Photoelectric effect: At low energies above 1 keV the photoelectric effect is dominant. The photon interacts with an electron and transfers its total energy. The previously bound electron is emitted from the atom after absorbing the energy [Her16]:

$$\gamma + \text{Atom} \longrightarrow (\text{Atom})^+ + e^-.$$

The excess energy of the photon after ionization is transformed into kinetic energy of the electron, while the recoil energy that is transferred to the atom can be neglected. The different peaks for the photoelectric cross section $\sigma_{p.e.}$, which can be seen in Figure 2.3, occur because with higher photon energies, stronger bound electrons can be ionized. The cross section is dependent on the atomic number Z and scales for the photoelectric effect between $\propto Z^4$ and Z^5 [Her16].

Compton scattering: The Compton scattering cross section $\sigma_{Compton}$ surpasses the photoelectric effect at intermediate energies (see Figure 2.3). This interaction is a semi-elastic scattering of a photon with an electron. The photon transfers part of its energy and momentum to the electron and changes its own. For photon energies above

the binding energy of the electron the Compton scattering scales with $\propto Z$ [Her16].

Pair production: The pair production cross section κ_e/κ_{nuc} is dominant at high energies as seen in Figure 2.3. In the process the whole energy of the photon is converted into an electron-position-pair. Therefore the threshold energy is twice the mass of an electron and the transferred recoil energy. For even higher energies the electron-positron-pair gains more momentum. The pair production happens most likely in the Coulomb-field of a nucleus. This process scales with $\propto Z^2$ [Her16].

In an energy range similar to the photoelectric effect, Figure 2.3 shows that also Rayleigh scattering $\sigma_{Rayleigh}$ is possible. This is an elastic scattering and transfers almost no energy into the material. Therefore, it is not interesting for particle detection [Her16].

2.2 Multi Wire Proportional Chamber

A Multi Wire Proportional Chamber (MWPC) is a gaseous type detector which is used for particle detection. It consists of a set of thin and equally spread anode wires placed between two cathode planes. Connecting a symmetric potential to the cathodes, while the anodes are grounded, results in an electric field as seen in Figure 2.4. The field lines show a constant behaviour except in the region close to the anode wires where the dependence is $\frac{1}{r}$ [Sau14].
The principle of the MWPC is based on the interaction of a particle with the chamber gas. During the ionization, positive charged gas ions are accelerated to the cathode plane, while the electrons are accelerated to the anode wires. Near the anode wires the velocity of the electrons increases significantly due to the electric field. The follow-up ionizations finally result in avalanche effects [Sau14]. The resulting current, collected by the anode, is proportional to the energy deposited in the detector by the particle [Rol08]. Another way of measuring the electron avalanche is by its induced mirror charge on the cathode plane [Her16]. The separation of the cathode plane into independent cathode pads enables a better localization of the avalanche, since the induced signal is a local effect [Her16]. One possible way to structure the cathode pads is shown in Figure 2.5

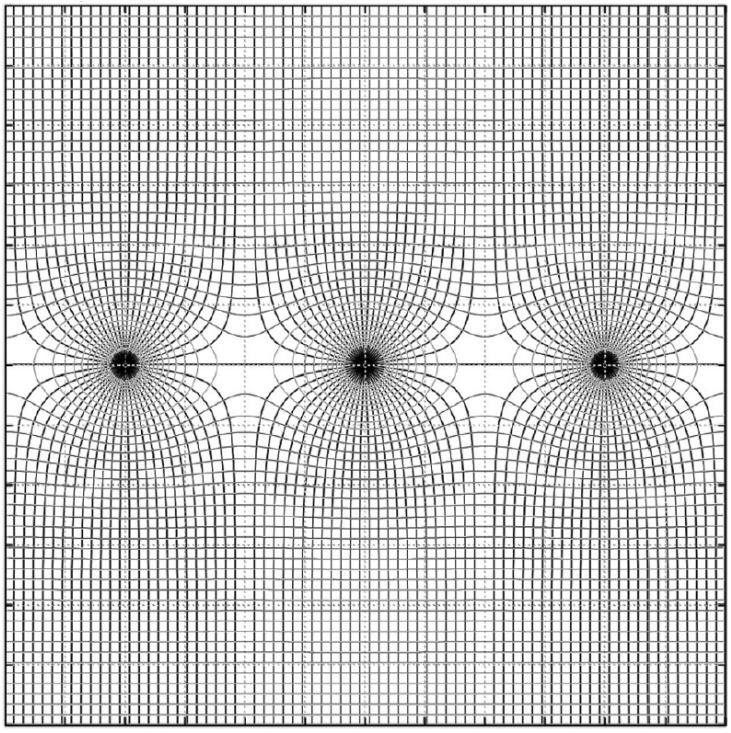

Figure 2.4: MWPC field lines and equi-potentials near the anode wires [Sau14].

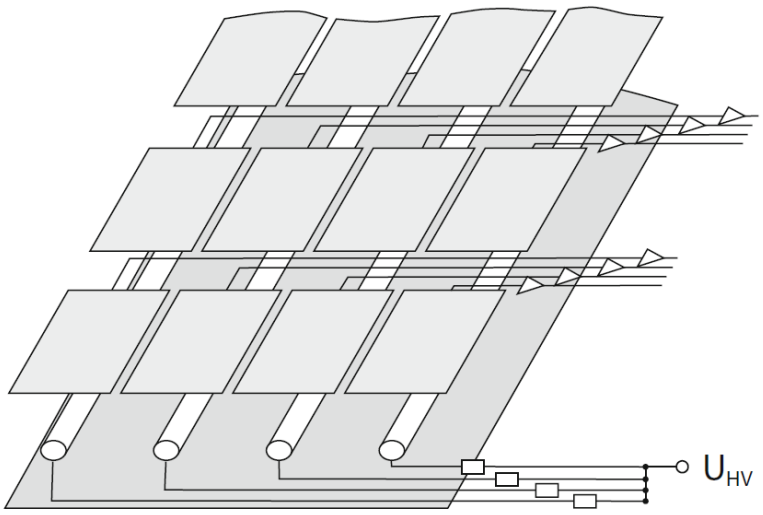

Figure 2.5: Principal of a MWPC with cathode pads [Her16].

The advantage of cathode pads is that analysing the distribution of the induced charge over the pads leads to a spatial resolution of the electron avalanche which is better than the geometric size of a single pad. Another important factor is the used gas for the MWPC and it varies for the different areas of application for the detector. By

using an inert noble gas, like Argon, one of the properties is a high ionization density, to name just a one [Her16].

2.3 Transition Radiation

Unless explicitly cited, the summary and equations in this chapter are reported from the following source [AW12].
A TRD consists of a radiator, which is a material that causes particles moving through the material to emit Transition Radiation (TR). The other thing needed is a particle detector, in the case of this thesis a MWPC, placed after the radiator to detect both, the energy loss of the particle and the emitted TR. This chapter will shortly summarize how TR is produced.
If a charged particle moving in the relativistic regime moves through an interface of two media with different dielectric constants ϵ_1 and ϵ_2, it emits a photon. This effect is called TR. The double differential energy spectrum, that is radiated, is dependant on the Lorentz factor γ and the dielectric constants of the two media and can be expressed as:

$$\frac{\mathrm{d}^2W}{\mathrm{d}\omega\mathrm{d}\Omega} = \frac{\alpha}{\pi^2}\left(\frac{\theta}{\gamma^{-2}+\theta^2+\xi_1^2} - \frac{\theta}{\gamma^{-2}+\theta^2+\xi_2^2}\right)^2. \tag{2.3}$$

Equation 2.3 holds for $\gamma \gg 1$, $\xi_1^2, \xi_2^2 \ll 1$, $\theta \ll 1$ and $\xi_i^2 = \omega_{Pi}^2/\omega^2$ with ω_{Pi} being the plasma frequency of the two media which depends on the electron density n_e and electron mass m_e of the material and α is the fine structure constant:

$$\omega_P = \sqrt{\frac{4\pi\alpha n_e}{m_e}}. \tag{2.4}$$

Since a medium has two interfaces with its surrounding medium and TR is produced when a charged particles crosses a interface of two media, the TR after leaving has to be taken into consideration. For a medium, for example a foil, both interfaces have to be taken into account:

$$\left(\frac{\mathrm{d}^2W}{\mathrm{d}\omega\mathrm{d}\Omega}\right)_{foil} = \left(\frac{\mathrm{d}^2W}{\mathrm{d}\omega\mathrm{d}\Omega}\right)_{interface} \cdot 4\sin^2\left(\frac{\phi_1}{2}\right). \tag{2.5}$$

Equation 2.5 sums the two interfaces up by adding a correction factor $4\sin^2\left(\frac{\phi_1}{2}\right)$, where the phase ϕ_1 is correlated to the formation length Z_i, the thickness l_i and can be approximated by:

$$\phi_i \simeq \frac{(\gamma^{-2} + \theta^2 + \xi_i^2)\omega l_i}{2\beta c}. \tag{2.6}$$

The so-called "formation zone" Z_i, shown in Equation 2.7, can be described as the distance after which the parent particle and the TR photon are separated. The formation zone depends on the particle's Lorentz factor and the energy of the TR photon as well as the emission angle of the TR, which is small for high γ and can be approximated with $\theta \simeq \sqrt{\gamma^{-2} + \xi_2^2} \approx 1/\gamma$. The TR yield is suppressed if the formation zone is much longer than the thickness l_i of the medium ($l_i \ll Z_i$).

$$Z_i = \frac{1}{\gamma^{-2} + \xi_i^2} \frac{2\beta c}{\omega} \tag{2.7}$$

Figure 2.6 illustrates a possible TR spectrum of a single interface and single foil configuration.

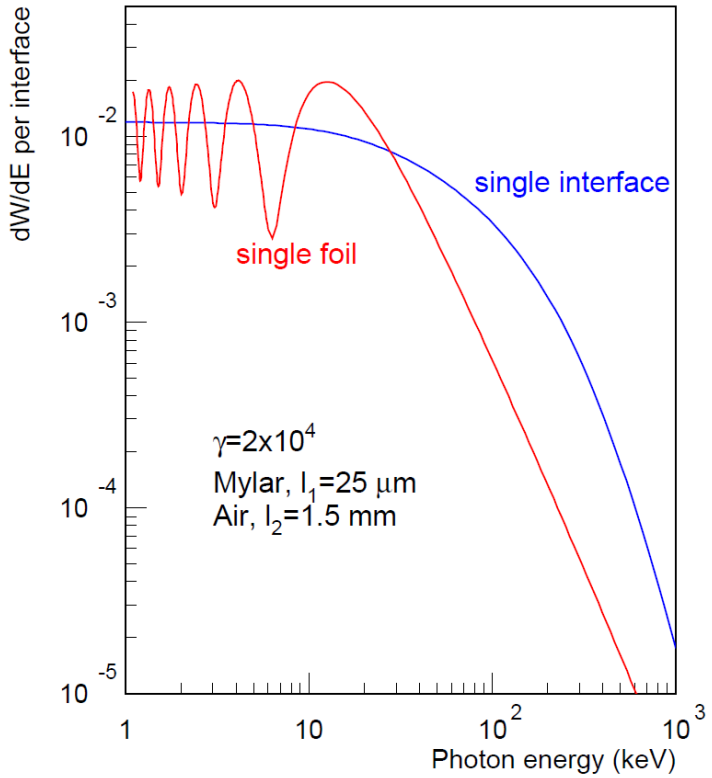

Figure 2.6: TR spectrum for a single interface (blue) and a single foil configuration (red) traversing between mylar and air [AW12].

3 Experimental Background

3.1 The CBM Experiment

In the future, the CBM experiment will study hadronic matter in the regime of intermediate temperatures and high net-baryon densities, as predicted by the QCD. To achieve this goal, the CBM experiment is designed and currently under construction at the FAIR at the GSI to be a high-intensity, heavy-ion experiment. In contrast to other experiments, CBM is designed for precise measurements of observables with low production cross sections, enabled by its high interaction rates. The CBM detectors are designed for event rates of up to 10 MHz. The SIS100 accelerator, which is currently under construction, will provide beam energies up to 29 GeV for protons, up to 11 AGeV for Au and for nuclei with $\frac{Z}{N} = 0.5$ up to 14 AGeV and intensities up to 10^9 Au ions per second [TDR18].

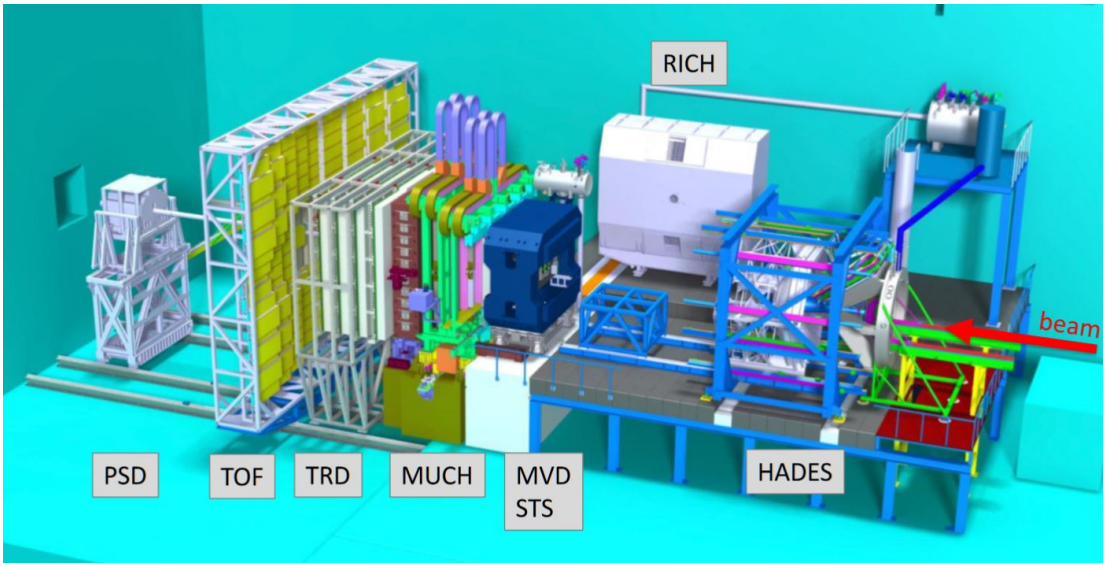

Figure 3.1: A render of the CBM experiment with labelled detectors and the beam direction from right to left [Her]. Instead of the PSD which is still drawn here, another centrality detector is currently in its design process for CBM.

Figure 3.1 shows a render of the different CBM detectors with the beam entering from the right side. In the following, the different detectors will be shortly described. More information can be found in[TDR18]. Starting at the target and going downstream the detectors are:

Micro-Vertex Detector (MVD)

The detector arrangement will resolve the position of secondary vertices with around 50 μm to 100 μm accuracy along the beam axis. The high resolution and low material budged detector consists of four layers of Monolithic Active Pixel Sensors (MAPS) detectors 5 cm to 20 cm downstream of the target.

Silicon Tracking System (STS)

This detector will provide track and momentum information of the charged particle. The system consists of silicon strip detectors which are located 30 cm to 100 cm downstream of the target and will provide a momentum resolution of around $\Delta p/p = 1.5\%$.

Ring Imaging Cherenkov Detector (RICH)

The RICH detector will be used for electron identification by measuring the Cherenkov radiation. In this case it will be a gaseous detector with focusing mirror elements and a photon detector. It will be set up 1.6 m downstream of the target with an overall length of approximately 2 m.

Muon Chamber System (MUCH)

This detector consists of multiple compact hadron absorber layers to track particles. It utilizes the information to perform a momentum dependent muon identification.

Time-Of-Flight System (TOF)

This detector unit will be used for hadron identification by means of the measured TOF, utilizes an area of about 120 m^2 and is placed about 6 m downstream of the target (for the SIS100). The time resolution has the order of 80 ps.

Projectile Spectator Detector (PSD)

This detector will be used to measure non-interacting nucleons and to determine the collision centrality as well as the orientation of the reaction plane. It is a lead-scintillator calorimeter and provides a uniform energy resolution.

3.2 The CBM-TRD

The CBM-TRD is an important detector for electron identification at momenta $p > 1 \frac{\text{GeV}}{\text{c}}$ for the CBM experiment. The design itself needed to fulfil certain requirements. An energy loss resolution better than 30% and a position resolution of about 300 μm is needed. Furthermore, the detector needs to have a pion suppression of 20 or better at an electron efficiency of 90%. As mentioned before the experiment works with high interaction rates and the design must be able to cope with the particle hit rates produced in 10 MHz interaction rate at the target with corresponding hit rates of up to 120 $\frac{\text{kHz}}{\text{cm}^2}$ at the TRD plane[TDR18].
This chapter briefly explains the used MWPC of the TRD and the part of the read out chain which is important for the framework discussed in chapter 4.
Figure 3.2 shows an exploded-view drawing of the CBM-TRD MWPC. The module consists of multiple layers. Particles enter through the Kapton foil and thereby move into the gas volume which contains a cathode wire plane and an anode wire plane followed by a Pad-plane. The Honeycomb and carbon layer as well as the aluminium frame ensure the structural strength [TDR18].

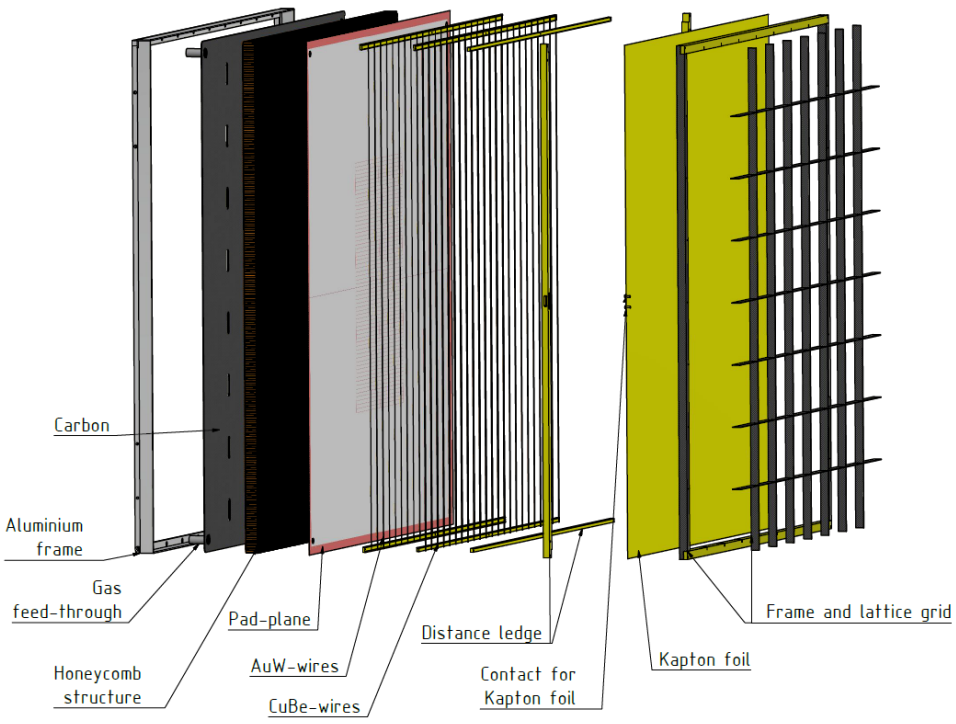

Figure 3.2: An exploded-view drawing of the CBM-TRD MWPC with visible layers. A particle would move through the module from right to left. [TDR18].

3.2.1 CBM-TRD MWPC

In addition to the amplification region the CBM-TRD MWPC is designed with an additional 5 mm drift region. The benefit of this addition is an increased absorption probability for TR and, in effect, an improved gas amplification stability against external pressure variations, while maintaining the signal collection below 0.3 μs.

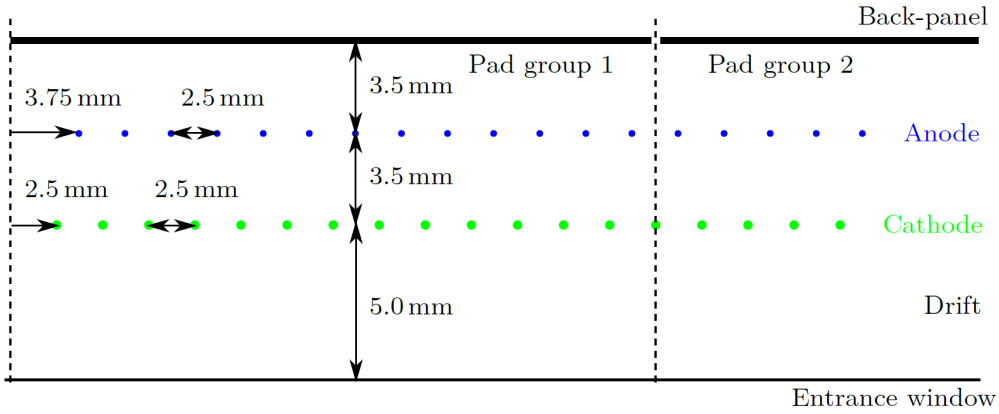

Figure 3.3: A schematic drawing of the wire pads of the CBM-TRD MWPC [TDR18].

Figure 3.3 shows a schematic drawing of the MWPC with the entrance window at the bottom, followed by the drift region to the 3.5 mm + 3.5 mm amplification region and ending with the back panel. In addition to the working principle explained in chapter 2.2, the ionization electrons drift to the cathode without an avalanche effect before entering the amplification region with a much higher electric field. The gas amplification is dependent on the voltage applied to the wires and the gas itself. For the standard operation of the CBM-TRD, a gas mixture of Xe/CO_2 (85/15) with a drift voltage of -500 V and an anode voltage of 1850 V were taken [TDR18]. As mentioned in chapter 2.2, the charge is measured by the induced mirror charge on the pad plane, which distributes according to the Pad Response Function (PRF).

3.2.2 Pad Response Function PRF

The PRF approximates the induced charge fraction of a pad as a function of the displacement with regard to the main pad. It is not a continuous measurement of the distributed charge over a pad but a discrete measurement for each pad by integrating the charge over a certain area. The PRF can be written as [TDR18]:

$$\begin{aligned}\mathrm{PRF}(d/h) &= \int_{d/h+W/2}^{d/h-W/2} \rho(d'/h)d(d'/h) \\ &= -\frac{\arctan\Big(\sqrt{K_3}\tanh\Big(\pi(\sqrt{K_3}-2)\cdot\frac{W-2\cdot d}{8h}\Big)\Big)}{2\arctan(\sqrt{K_3})} \\ &\quad -\frac{\arctan\Big(\sqrt{K_3}\tanh\Big(\pi(\sqrt{K_3}-2)\cdot\frac{W+2\cdot d}{8h}\Big)\Big)}{2\arctan(\sqrt{K_3})},\end{aligned} \tag{3.1}$$

where K_3 is a chamber geometry factor of the MWPC, W is the pad width, h is the distance between the anode wire and pad plane and d is the displacement of the charge cluster relative to the main paid centre [TDR18]. The charge density distribution $\rho(d/h)$ describes the induced charge closely located around a location on the pad plane where a particle moved through the detector [TDR18]:

$$\rho(d/h) = q_a \frac{\frac{\pi}{2}\cdot\left(1-\frac{\sqrt{K_3}}{2}\right)\sqrt{K_3}}{4\arctan(\sqrt{K_3})}\cdot\frac{1-\tanh^2\left(\frac{\pi}{2}\cdot\left(1-\frac{\sqrt{K_3}}{2}\right)\frac{d}{h}\right)}{1+K_3\tanh^2\left(\frac{\pi}{2}\cdot\left(1-\frac{\sqrt{K_3}}{2}\right)\frac{d}{h}\right)}. \tag{3.2}$$

Equation 3.1 is important to calculate the pad charge distribution for every single pad, executed in the following analysis.

3.2.3 Readout Chain

The detector read out is done by using the Self-triggered Pulse Amplification and Digitisation ASIC (SPADIC) readout chip. Figure 3.4 shows a conceptional diagram of the SPADIC. The chip itself contains 32 analogue input channels that are divided into two 16 channels half chips, therefore being able to read out 32 pads of the MWPC in parallel. The channels consist of multiple parts, the first one being the Charge Sensitive Amplifier (CSA), followed by an Analog-to-Digital Converter (ADC), a programmable Digital Signal Processor (DSP) and a hit detection logic [TDR18].

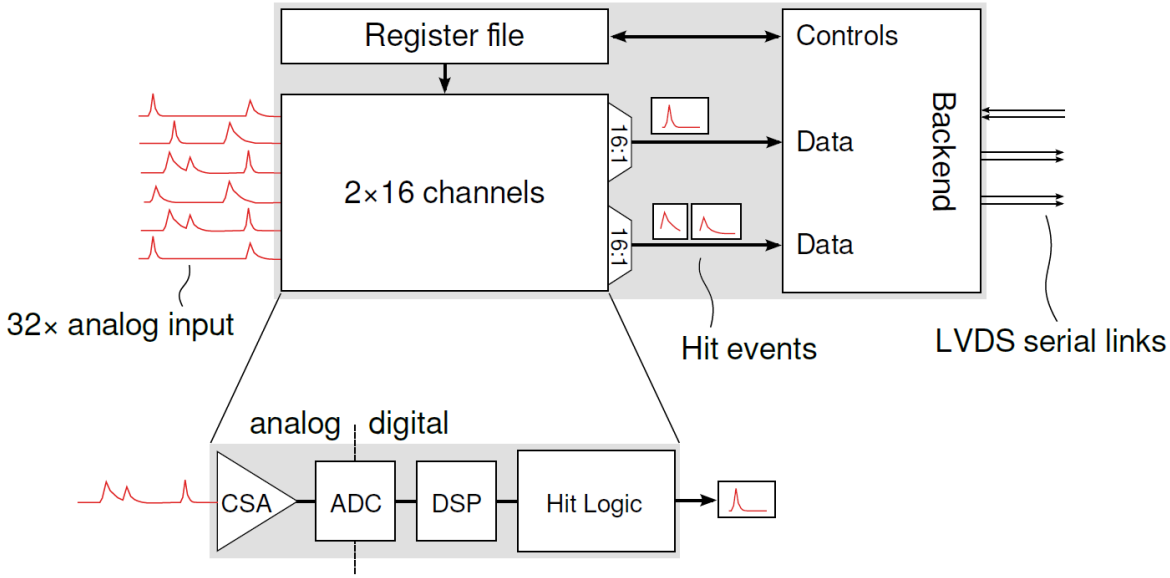

Figure 3.4: Conceptional diagram of the SPADIC [TDR18].

The CSA plays an important role in the simulation framework of this thesis. When a particle passes through the detector, the incoming charge on the pads is amplified by the CSA's amplifier and the integrated shaper generates a pulse that can be described by equation 3.3 [TDR18]:

$$f(t) = A \cdot \frac{t}{\tau} \cdot \exp\left(-\frac{t}{\tau}\right) \qquad (\text{for } t \geq 0). \tag{3.3}$$

From equation 3.3 follows that the amplitude A is dependent on the initial charge of the signal, while the peaking time of the pulse is given by $\tau = 240\,\text{ns}$. After the CSA, the pulse is digitized by the ADC which is continuously sampling with a sampling frequency of 16 MHz, resulting in a sample step length of 62.5 ns. With an ADC sampling resolution of 9-Bit, the sample values have a range from -256 to 255 [TDR18]. Figure 3.5 shows a schematic drawing of the pulse shape (a) before sampling and (b) after sampling, as described by equation 3.3.

After the DSP, the digitized signal is transferred to the hit detection logic. The SPADIC is a self-triggered chip, which decides whether a signal should be saved or not. This leads to different trigger types to separate pulses which do themselves fulfil the trigger condition from those which are co-triggered from the pad neighbour in order to see the full PRF. This information is transferred to the hit message [TDR18].

(a) **(b)**

Figure 3.5: Schematic drawing of the pulse shape (a) with sample steps (b) [Arm13].

The SPADIC is operated on the Front-End-Boards (FEB), that is mounted to the back of the chamber. After the front-end, the data is send to the Read-Out Board (ROB), combining the data from the different SPADICs, where it is send to the FPGA based receiver cards (Common Readout Interface (CRI)) for data pre-processing. After this, the data is send to the First Level Event Selector (FLIB/FLES) for storage and analysis [TDR18]. For detailed information about the Readout Chain, see [TDR18].

4 Simulation Framework

This chapter is comprised of how the Signal Simulation Framework works. The main goal of the framework is to model the behaviour of the energy and spatial resolution as well as the range of fluctuations of the signal path in dependency of different types of uncertainties and reconstruction methods. This should allow for a better understanding of the uncertainties of the real charge values and offer a possibility to compare different reconstruction methods. The simulation offers a high flexibility concerning methods and full control on introducing supposed signal characteristics like cluster charge, displacement, sampling phase, sampling step size, peaking time, chamber geometry and uncertainties, thereby potentially exceeding the level of probing compared to the simulations within Cbmroot. Figure 4.1 shows the simplified functionality of the framework in form of a flow chart.

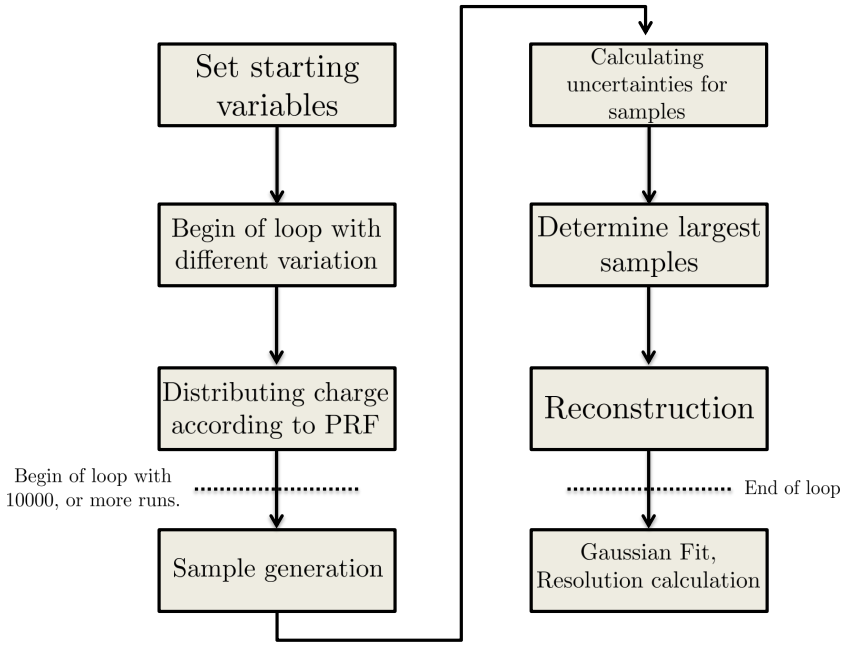

Figure 4.1: Simplified flow chart of the Signal Simulation Framework for the CBM-TRD.

The framework has two main ways of operation. The first one is the variation of incoming energy with a fixed position, while the other one is the variation of displacement with a fixed energy. After that the PRF is calculated according to equation 3.1 and, due to the idealized conditions of a simulation framework, it is constant for the whole hit generation. In the later analysis, the PRF was operated with the chamber geometry factor $K_3 = 0.38$, a pad width $W = 7.125\,\text{mm}$ [Ber14] and the pad plane to anode wire plane distance $h = 3.5\,\text{mm}$ [TDR18].
For every change in the variation variable, 10000 hits are simulated and every hit has its cluster charge varied. This appeared to be a good compromise between statistics and runtime for the simulation. At this point, right before the generation of the samples, the first Simulated Uncertainty SU1 is incorporated (see below). Every channel (pad) generates 32 samples, calculated with a 62.5 ns sampling step using equation 3.3. The amplitude A was set in such a way that it is the maximum value of equation 3.3.
Next in line is the generation of uncertainties. The uncertainties itself are generated with a random generator utilizing a Gaussian distribution. The random generator is a TRandom3 from root. There a three different types of uncertainties that will be discussed in this thesis.
Simulated Uncertainty 1 (SU1) is proportional to the incoming charge. It shall display the fluctuations of gas amplification and registration [Sau14]. It is applied in common to all signals from a charge cluster, thereby to the overall charge value. SU2 is an absolute uncertainty, thereby independent on the charge signal height. It models fluctuations of the analogue front-end and of the ADC ("sample-to-sample fluctuations"). This is generated newly and independently for every sample and every pad. The last one is SU3, which is an absolute uncertainty and describes a potential oscillation of the whole system due to background effects. SU3 is identical for all pads for one hit and is modelled with

$$f(x) = A \cdot \sin(\omega t + \varphi_0). \tag{4.1}$$

The amplitude A and phase φ_0 are determined by a random generator and change for every hit.
Since the framework uses ADC Units for the energy values, the next step determines the sample with the highest ADC Unit value (Max ADC), due to the fact, that the reconstruction methods are centred around the sample with the largest value.
There are four reconstruction methods:

- Method 1 (Max. ADC): The Max ADC of the main pad and its corresponding neighbour pads are added together.
- Method 2 (3 Samples): The Max ADC with one sample before and after the Max ADC of the main pad and its corresponding neighbour pads are added together. Example: If sample 6 is the Max ADC sample, than the samples $5-7$ are added up.
- Method 3 (5 Samples): The Max ADC with two samples before and after the Max ADC of the main pad and its corresponding neighbour pads are added together Example: If sample 6 is the Max ADC sample, than the samples $4-8$ are added up.
- Method 4 (Integral): All samples of the main pad and its corresponding neighbour pads are added together.

The reconstructed-true is Gaussian distributed, therefore the end result is fitted with an Gaussian fit after the hit loop is finished. The resolution is calculated by using the fitted parameters μ and σ.
The spatial resolution was done by using the Centre-of-Gravity approach (equation 4.2) for the idealized and uncertain samples and comparing the reconstructed location of the hit:

$$d = \frac{\sum Q_{Pad} \cdot s_{pp} \cdot W}{\sum Q_{Pad}}. \tag{4.2}$$

Equation 4.2 describes the position of the hit dependent on the involved pads with the pad charge Q_{Pad} and the pad position s_{pp} relative to the main pad.

Remark: To describe the statistical uncertainties of the simulation a deeper look at the fit parameters was taken. The statistical uncertainties of the fit parameters were in all cases negligible. Furthermore, is the simulation framework stable for the same setting. The difference in the fit parameters for different simulations, regarding the same parameters, had a magnitude of around 10^{-5} to 10^{-6}.

5 Results

This chapter provides the results of the simulation showing the effect of uncertainties depending on the method applied for extraction of values, i.e., of deposited charge and hit position. First, the energy resolution will be discussed with the variation of incoming energy and displacement followed by the spatial resolution.

5.1 Energy Resolution

5.1.1 Variation of incoming Energy (A)

This part describes the cluster charge dependency of the resolution. Figure 5.1 shows the resolution of different methods with the variation of the cluster charge and only using SU1 and SU2, because they are the basically expected uncertainties and were set to SU1 = 6% of the incoming charge as Gaussian width and SU2 = 3 ADC Units. For a cluster charge of 100 ADC Units, Figure 5.1 shows a difference in the resolution of 0.9 percent points, with Method 4 being the best one at 6.12% and Method 3 the worst at 7.02%. The difference in resolution becomes smaller and better for all methods except Method 4, which approximately stays the same, for increasing cluster charges until a critical region of around 270 ADC Units. At this point, the resolution gets worse for all the methods until the peak at around 345 ADC Units with a maximum of approximately 6.8% for Method 1, while the other methods stay around 6.2%. For large cluster charge values the resolution reaches a plateau around 6%. Figure 5.2 shows the same behaviour for low cluster charges and reaches the same plateau for intermediate cluster charges. The difference between both is that Figure 5.2 was restricted to three pads only, meaning that the reconstruction only utilized the main pad and the corresponding neighbour pads, ignoring the additionally triggered side-pads, which would lead to a charge loss of around 0.2% of the incoming charge.

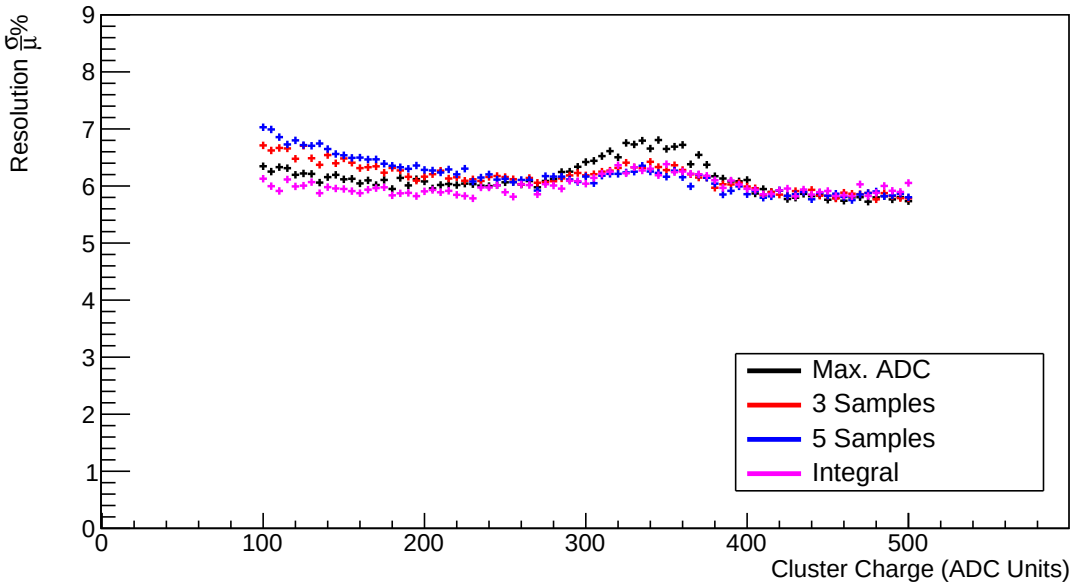

Figure 5.1: Resolution of cluster charge in dependence of cluster charge with SU1 = 6% and SU2 = 3 ADC Units.

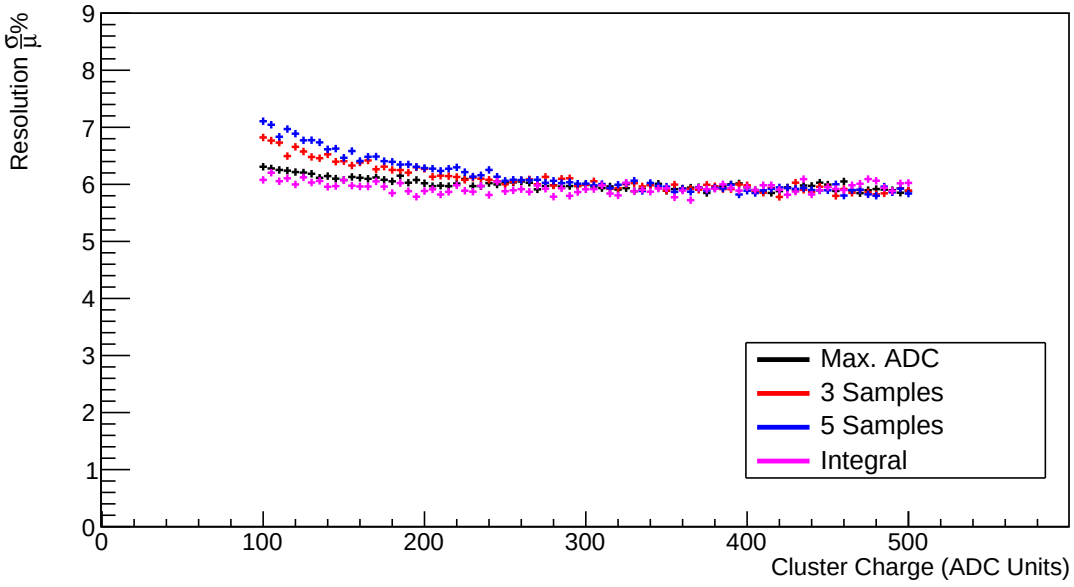

Figure 5.2: Resolution of cluster charge in dependence of cluster charge with SU1 = 6% and SU2 = 3 ADC Units while limited to 3 Pads

The next part was to determine weather the mean μ, sigma σ or both parameters are affected by the uncertainties. Figures 5.3 and 5.4 show the dependency for mean and sigma, respectively. Since the resolution is proportional to sigma and inverse proportional to the mean it takes a smaller mean or a higher sigma, compared to the optimal case, to obtain a worse resolution. The mean is proportional to the incoming cluster charge and as derived by Figure 5.3, the uncertainties have no effect on it, leaving sigma to be the main parameter affected by the uncertainties as shown in Figure 5.4. At the lower cluster charge range, Figure 5.4 shows the reason for the behaviour of Method 3 in Figure 5.1. Method 3 is worse for low charge clusters compared to the other methods because of the working principles of the reconstruction itself. At the low range of 100 ADC Units the fraction of the overall charge seen by a neighbour pad is even smaller. If the uncertainties are large enough to shift the largest sample to a different position, the adjacent samples will contribute less to the reconstructed cluster. This occurrence does not effect Method 1 or 4 and is significantly less effective for Method 2. With a larger cluster charge, the position of the highest sample is stabilized as seen by the recovery of sigma in Figure 5.4. Another point is that Method 4 has a much higher sigma and effect on sigma than the other three methods, but it can compensate these effects by an also much higher mean resulting in a better resolution.
Taking a more detailed look at the effect of the different uncertainties, Figures 5.5 and 5.6 portray the resolution for different cluster charge variations with only SU1 at 6%. As expected, the resolution is close to 6% regardless of the number of pads triggered. Since SU1 describes the fluctuation of the gas amplification, it is the upper limit for the resolution as shown below. For an ideal simulation with only SU1, Method 4 shows a rather strong fluctuation around 6% compared to the other methods. The reason for this is the digitization of the signal samples to integer numbers. Anyhow, this effect is negligible as soon as more uncertainties are added to the system.

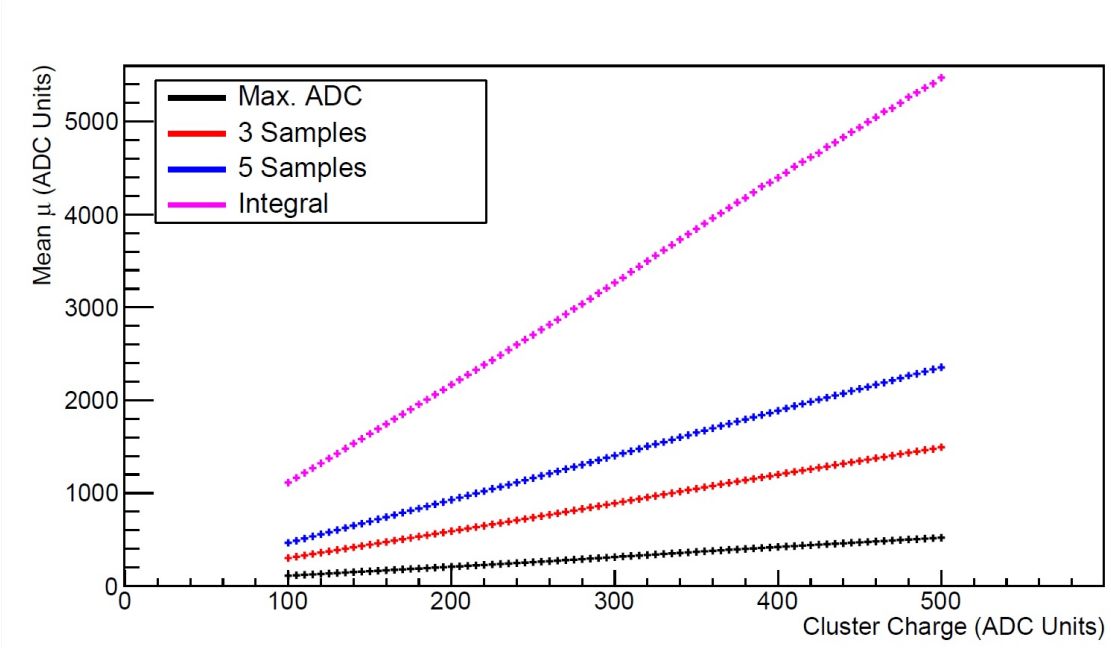

Figure 5.3: Mean dependency. Cluster charge variation with SU2 = 3 ADC Units.

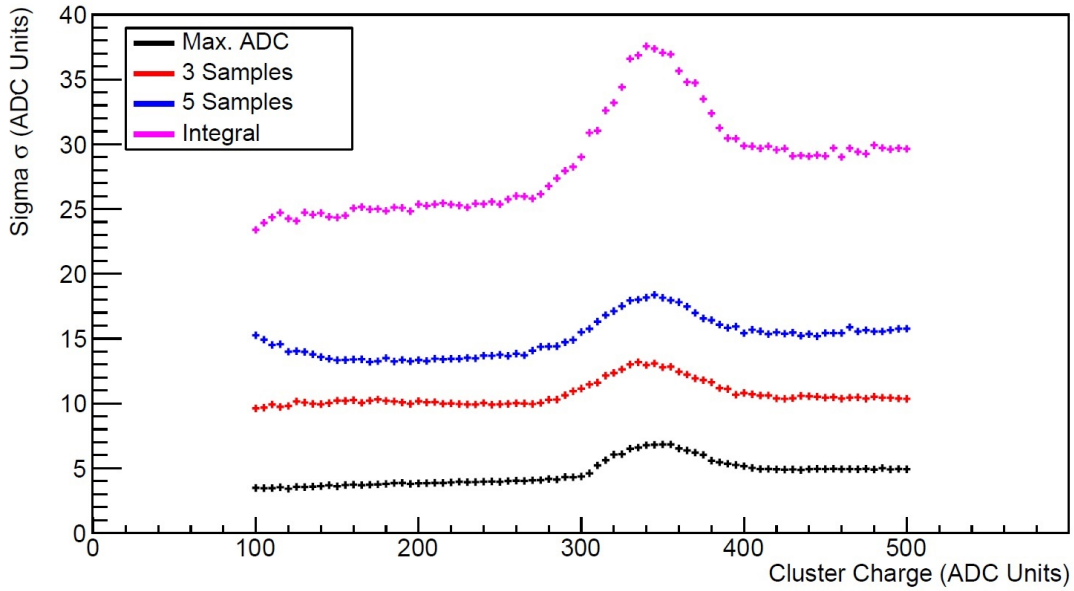

Figure 5.4: Sigma dependency. Cluster charge variation with SU2 = 3 ADC Units.

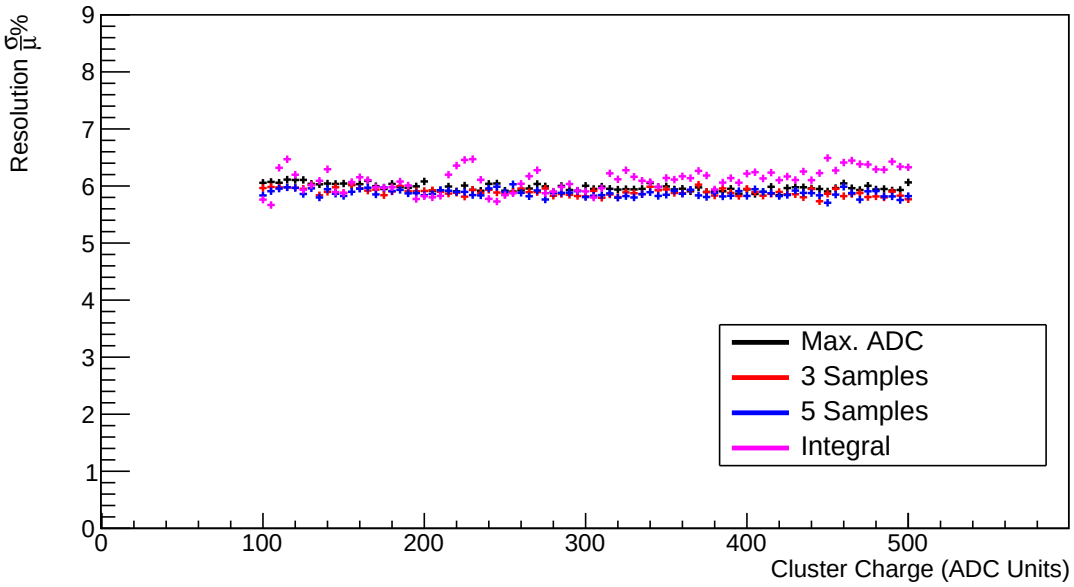

Figure 5.5: Resolution of cluster charge in dependence of cluster charge with SU1 = 6%.

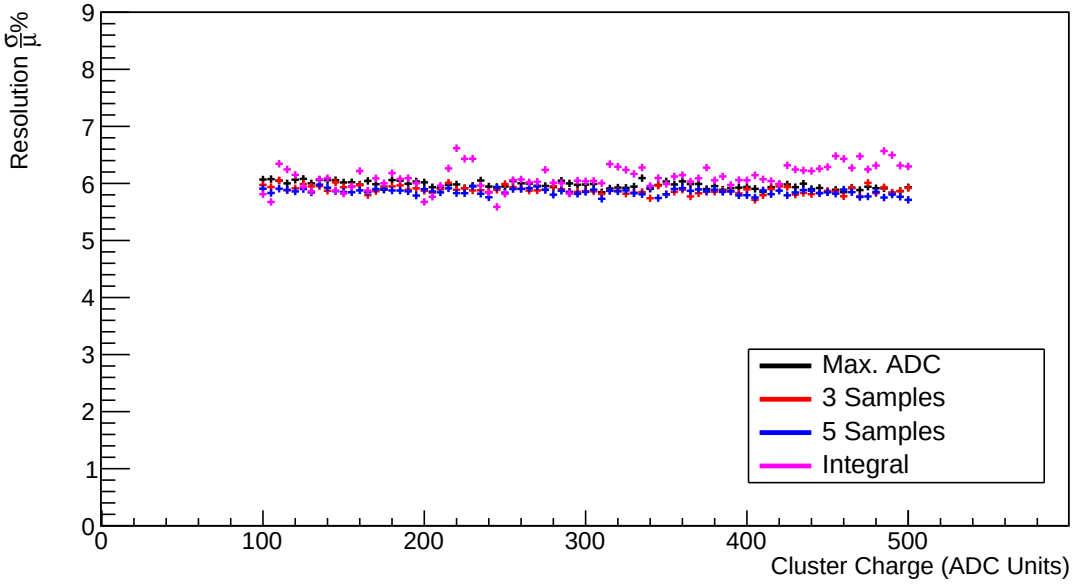

Figure 5.6: Resolution of cluster charge in dependence of cluster charge with SU1 = 6% while limited to 3 Pads.

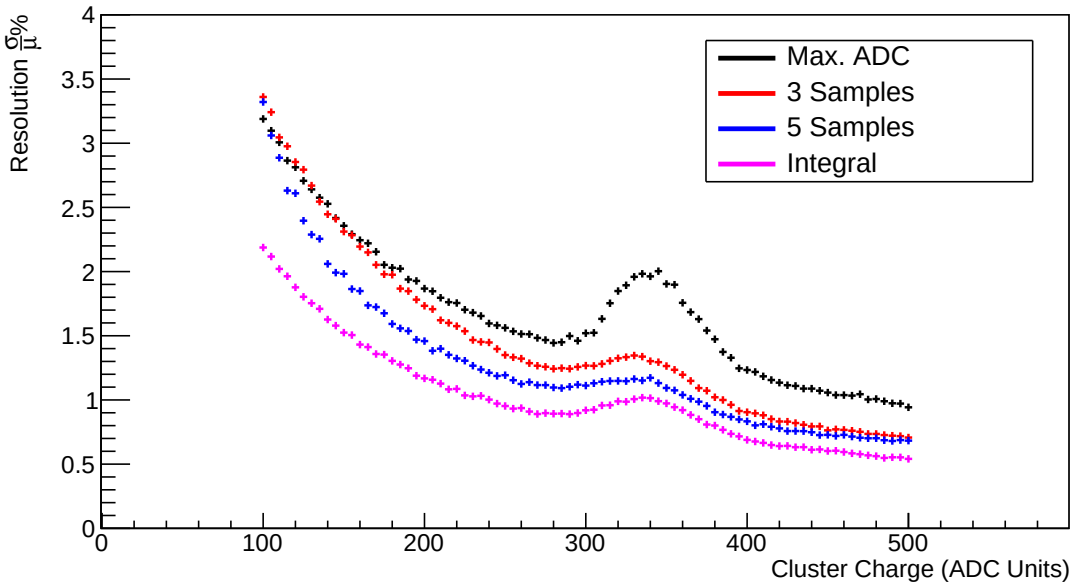

Figure 5.7: Resolution of cluster charge in dependence of cluster charge with SU2 = 3 ADC Units.

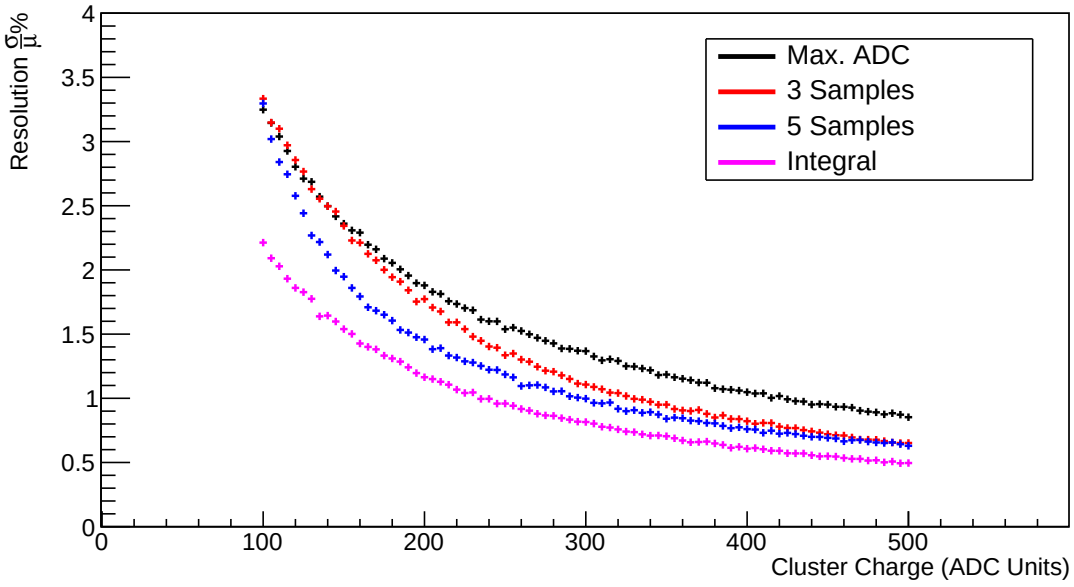

Figure 5.8: Resolution of cluster charge in dependence of cluster charge with SU2 = 3 ADC Units while limited to 3 Pads.

The effects of SU2 are portrayed by Figures 5.7 and 5.8 with only three pads. For low cluster charges, Method 4 at 2.18%, shows a better resolution than the other methods at around 3.3%. The course of the graphs shows that the resolution improves more for reconstruction methods with a higher number of samples, with Method 4 being the best one throughout the total range, after increasing the incoming cluster charge value. Like in Figure 5.1, the resolution gets worse after more pads are triggered at around 290 ADC Units, a bit later than with SU1 and SU2 combined. Method 1 is clearly the one affected the most by this uncertainty and shows a deterioration of resolution of approximately 0.6 percent points while the other methods lay around 0.15 percent points in the range of 290 ADC Units to 340 ADC Units. Even at higher cluster charges Method 1 does not reach the resolution of the other methods due to the fact that SU2 is an independent, absolute uncertainty and Method 1 utilizes only one sample for the reconstruction. In contrast to that, Method 4 is the best method utilizing all samples. Since Method 1 is the one affected the most by SU2, Figure 5.9 shows the effect of the uncertainty ranging form 1 ADC Units to 6 ADC Units. The overall resolution deteriorates drastically for higher uncertainties especially at low cluster charges and intermediate charges with more than three pads. At 100 ADC Units, the resolution jumps from 1.46% to 5.35% by changing SU2 to 6 ADC Units. Another effect is that the cluster charge needed to trigger more than three pads decreases with increasing SU1 from around 340 ADC Units to 220 ADC Units, while also increasing the worsening effect of the uncertainty. For 6 ADC Units, the difference in resolution for three pads is around 1 percent point and has a range of 180 ADC Units for the cluster charge to compensate the effect.

In the following simulations, also SU3 is enabled with an amplitude of 5 ADC Units and a frequency of 2.2 MHz. It adds an oscillating component to the signals, as indications for such were observed in real signal studies [Käh20]. Figure 5.10 shows the behaviour of the resolution with all three uncertainties applied. The overall resolution gets worse with Method 4 still being the best option, but Method 3 is no longer the worst option for low cluster charges. At 100 ADC Units Method 4 has a resolution of 6.83% while the other methods are around 7.7%. The peak after triggering more than three pads is higher for all methods than before and reaches around 7.8% for Method 1 and 6.7% for Method 3 and 4, while the critical region to trigger more than three pads has shifted to around 260 ADC Units. For higher cluster charges the resolution converges again to 6%.

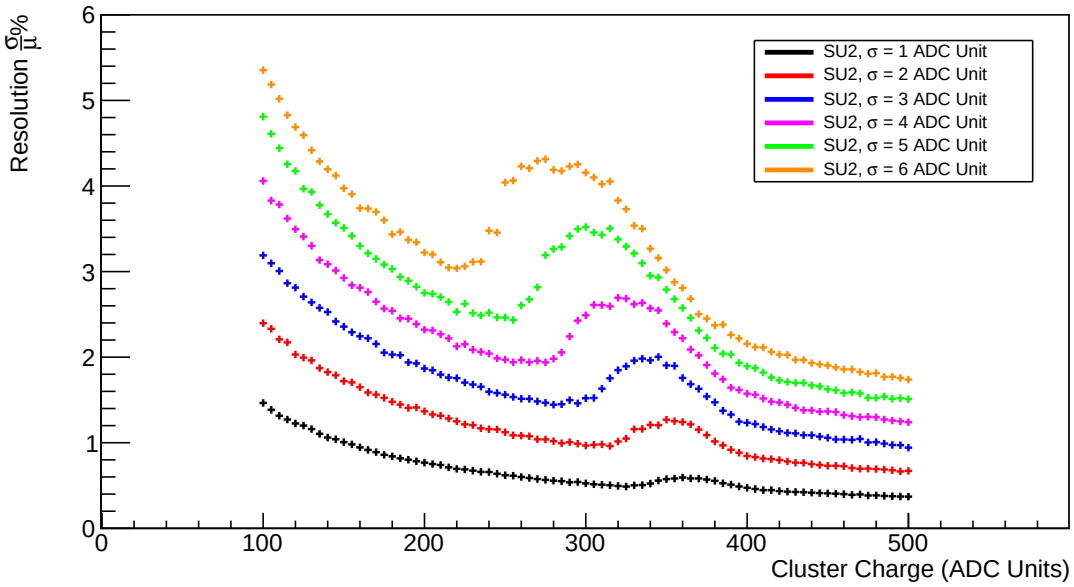

Figure 5.9: Resolution of cluster charge in dependence of cluster charge with SU2 ranging from 1 ADC Unit to 6 ADC Units using reconstruction method: Max. ADC.

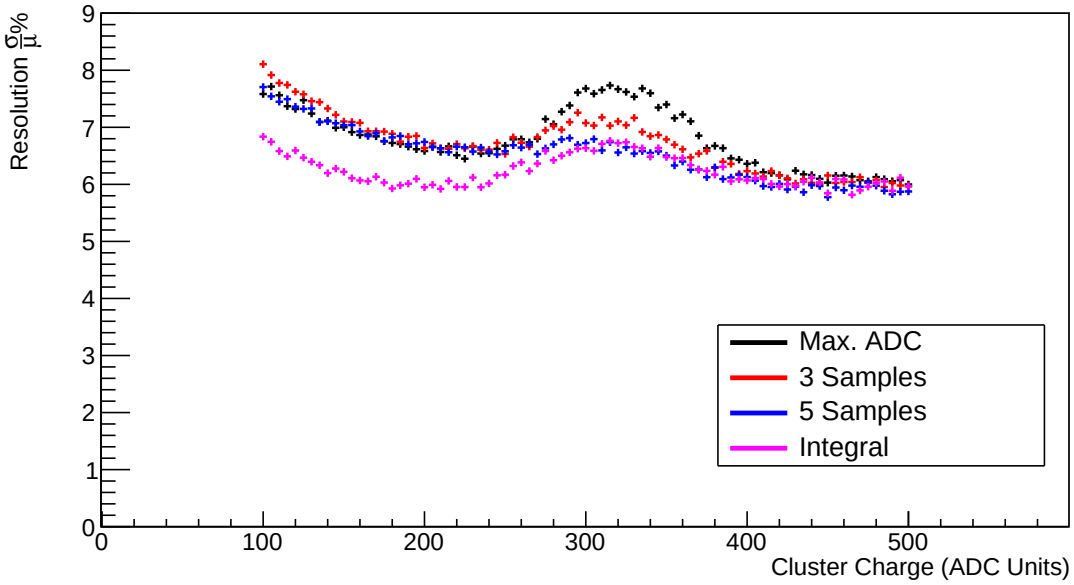

Figure 5.10: Resolution of cluster charge in dependence of cluster charge with SU1 = 6%, SU2 = 3 ADC Units and SU3 with $A = 5$ ADC Units.

The effect of SU3 on the different reconstruction methods is shown in Figures 5.11 and 5.12 with and without pad limitation, respectively. Since SU3 is an oscillating uncertainty and identical for all pads for one hit, the uncertainties add up over the pads. As mentioned before, Method 1 is susceptible for absolute uncertainties and therefore, Figure 5.11 shows fluctuations in the resolution for Method 1 and 2 for low cluster charges. Even if Method 3 is in the same region as the other two, it has a more stable behaviour like Method 4. Again a deterioration can be seen at about 330 ADC Units leading to a resolution of around 3% for Method 1 and 2. Interesting is the behaviour of Method 3 and 4 at this critical range. While Method 3 only deteriorates by around 0.35 percent points, Method 4 deteriorates by around 0.8 percent points. Furthermore, for cluster charges higher than 370 ADC Units, Method 3 has a better resolution than Method 4, which could not regenerate the resolution in the simulated range. As soon as the reconstruction is limited to three pads, Method 4 offers the best resolution as seen in Figure 5.12.

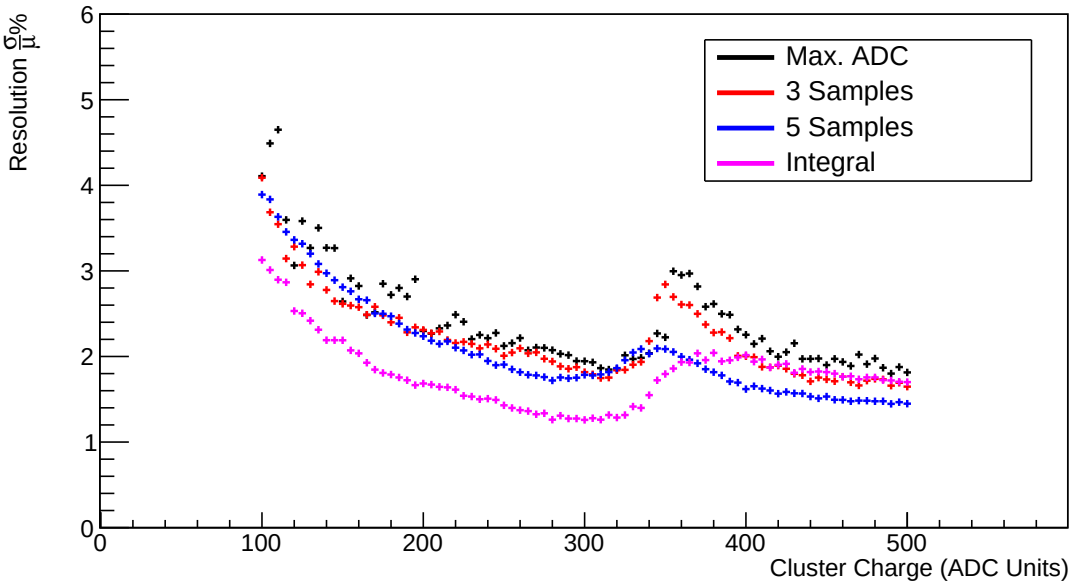

Figure 5.11: Resolution of cluster charge in dependence of cluster charge with SU3 with $A = 5$ ADC Units.

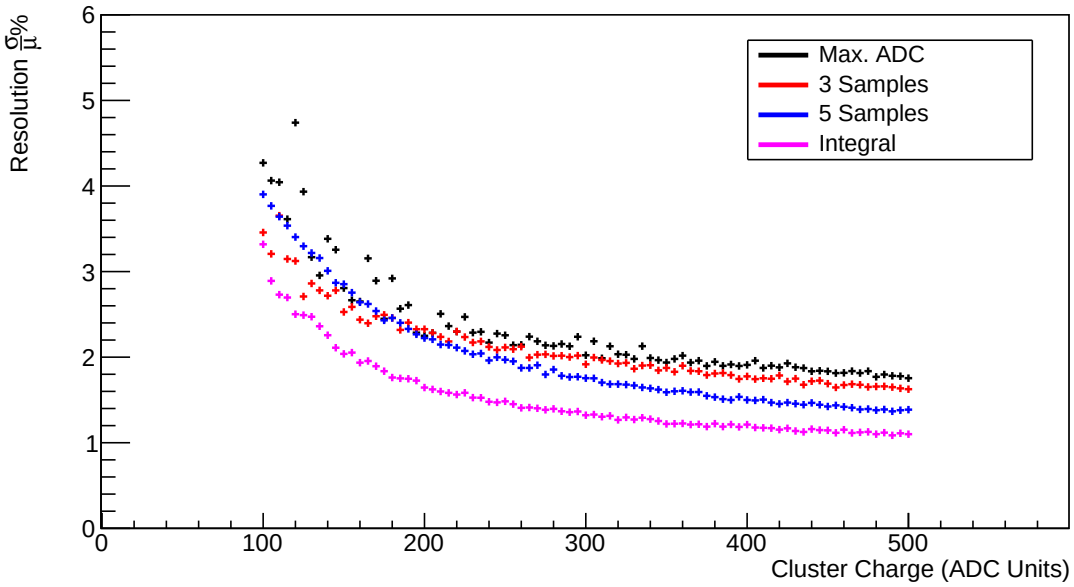

Figure 5.12: Resolution of cluster charge in dependence of cluster charge with SU3 with $A = 5$ ADC Units while limited to 3 Pads

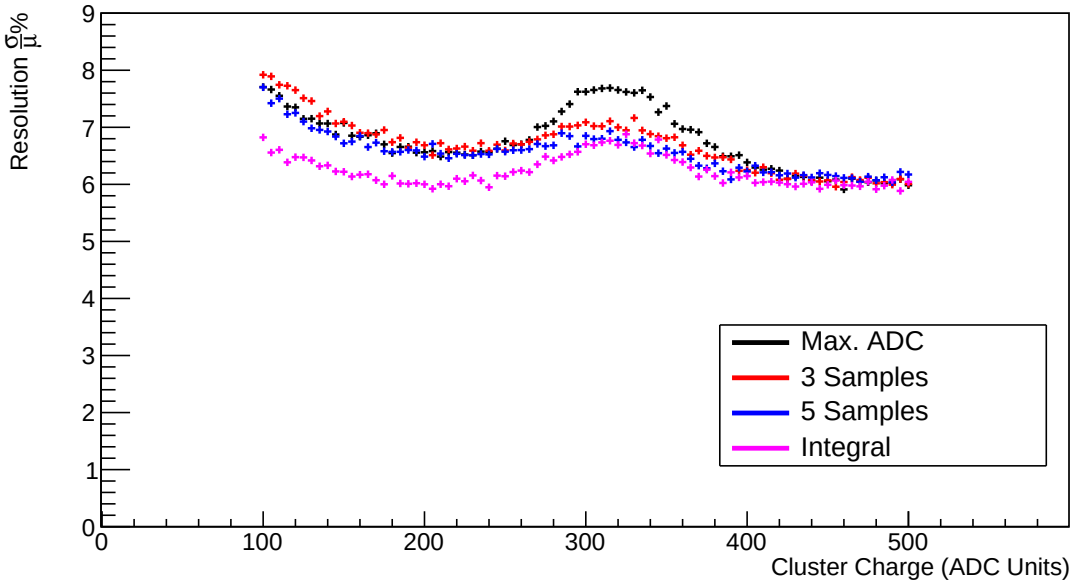

Figure 5.13: Resolution of cluster charge in dependence of cluster charge with SU1 = 6%, SU2 = 3 ADC Units, SU3 with $A = 5$ ADC Units and pulse shape phase of $\varphi = \pi$, meaning that the pulse shape is sampled between the optimal sample positions.

Finally, Figure 5.13 shows the resolution for all four reconstruction methods and uncertainties like Figure 5.10, with the difference that the samples were generated with a phase of $\varphi = \pi$ sampling between two optimal samples. The overall resolution stays the same and has only a slight to no effect on Method 1 and 4, while getting slightly better resolutions at low cluster charges and slightly worse resolutions for higher cluster charges with Method 2 and 3.

5.1.2 Variation of Displacement (d)

In this chapter, the position of the incoming hit is varied to analyse the effects of the uncertainties on non central hits. Figure 5.14 shows the resolution dependent on the displacement for the two uncertainties SU1 at 6% and SU2 with 3 ADC Units simulated with a cluster charge of 200 ADC Units. In comparison to Figure 5.1, the resolution is around 6% for all methods, with Method 3 being slightly worse, which can be traced back to the same explanation for small cluster charges as discussed before. Due to the position of the pads, the resolution shows a symmetrical behaviour around the central position. Therefore, only the positive displacement will be discussed. After around 0.6 mm, the resolution begins to deteriorate as more pads are triggered, which can not be seen in Figure 5.15. At around 1 mm, the peak of 6.8% is reached with all methods close together, with Method 4 still being the best one. The resolution is able to recover quickly and reaches its plateau of 6% after around 1.2 mm again. Figure 5.16 shows the resolution under the condition of the same uncertainties, but with a cluster charge of 330 ADC Units. The difference is that 330 ADC Units in the centre of the critical region seen in Figure 5.1. The worst resolution of around 6.6% shows up for all methods at the central position. While Method 1 is the worst around the centre, all methods become almost indistinguishable after a displacement of 0.5 mm. The difference between the triggered pads is that in Figure 5.16 are five pads triggered right away, while Figure 5.14 displays the effect of a fourth pad being triggered. For lower cluster charges this happens at a higher displacement.
Looking a little more into detail for each uncertainty, Figure 5.17 shows the resolution with only SU1 at 6%. Like the chapter before, SU1 describes the limit for the resolution and all methods are equally good.

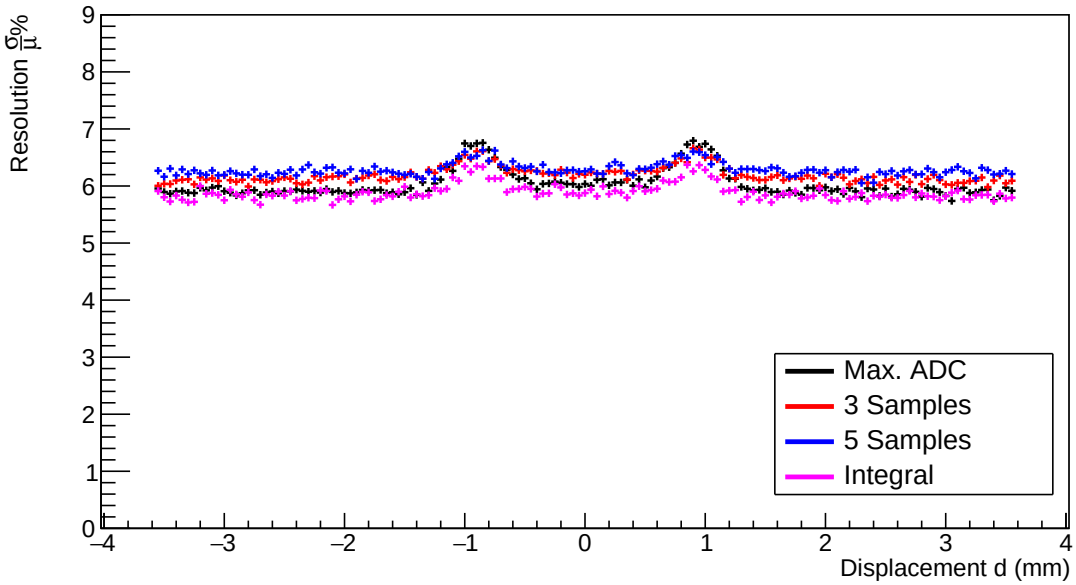

Figure 5.14: Resolution of cluster charge in dependence of displacement with SU1 = 6%, SU2 = 3 ADC Units and a cluster charge of 200 ADC Units.

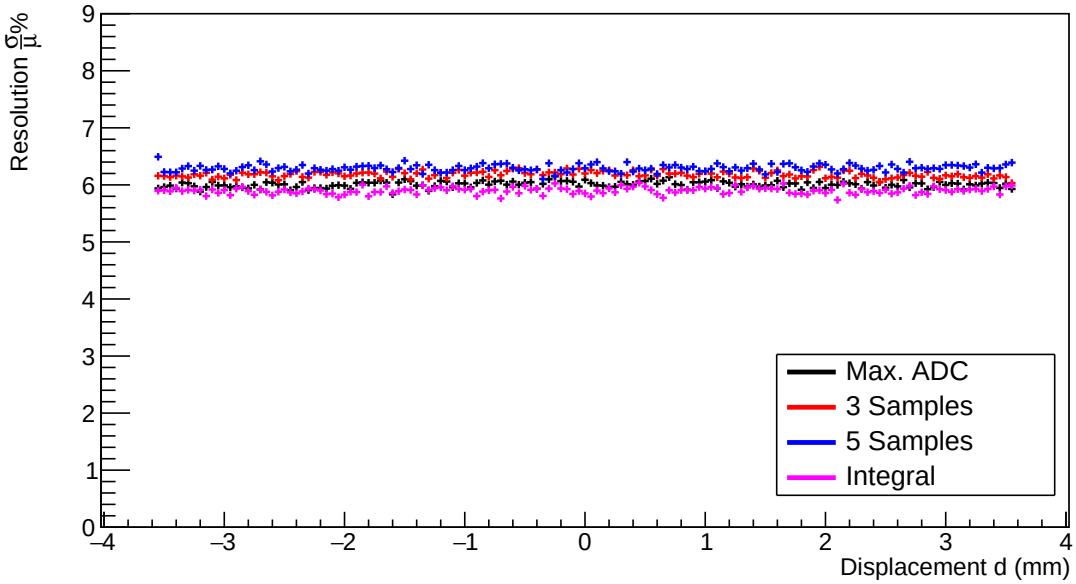

Figure 5.15: Resolution of cluster charge in dependence of displacement with SU1 = 6%, SU2 = 3 ADC Units while limited to 3 Pads and a cluster charge of 200 ADC Units

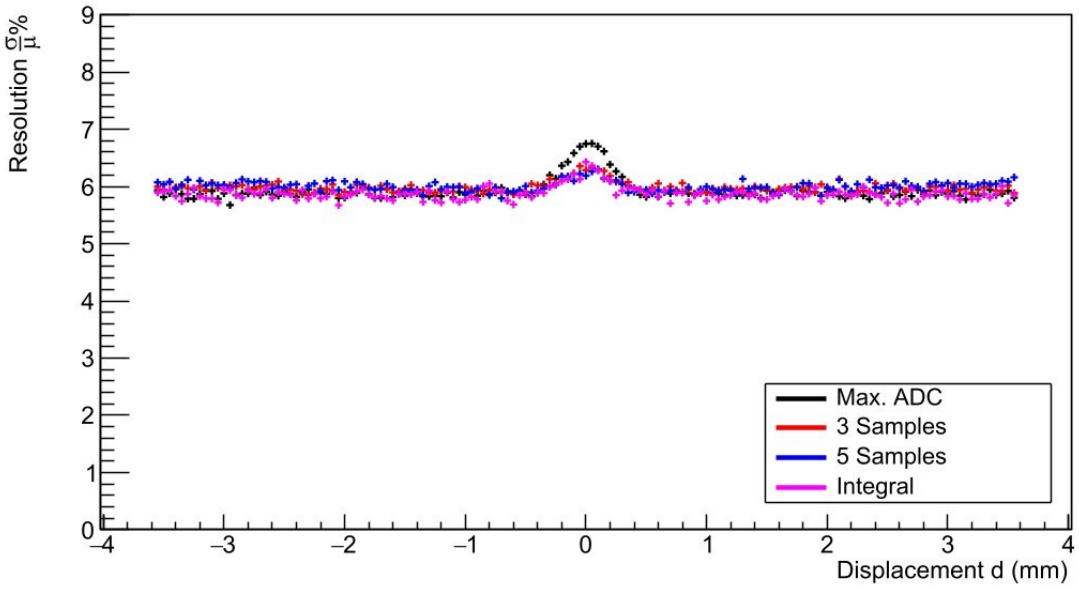

Figure 5.16: Resolution of cluster charge in dependence of displacement with SU1 = 6%, SU2 = 3 ADC Units and a cluster charge of 330 ADC Units.

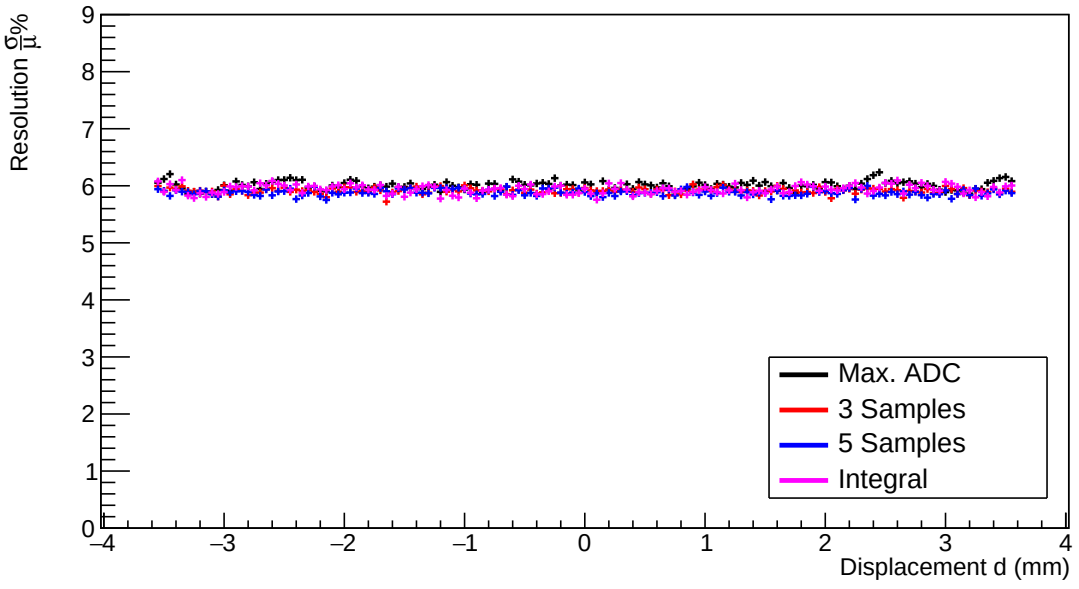

Figure 5.17: Resolution of cluster charge in dependence of displacement with SU1 = 6% and a cluster charge of 200 ADC Units.

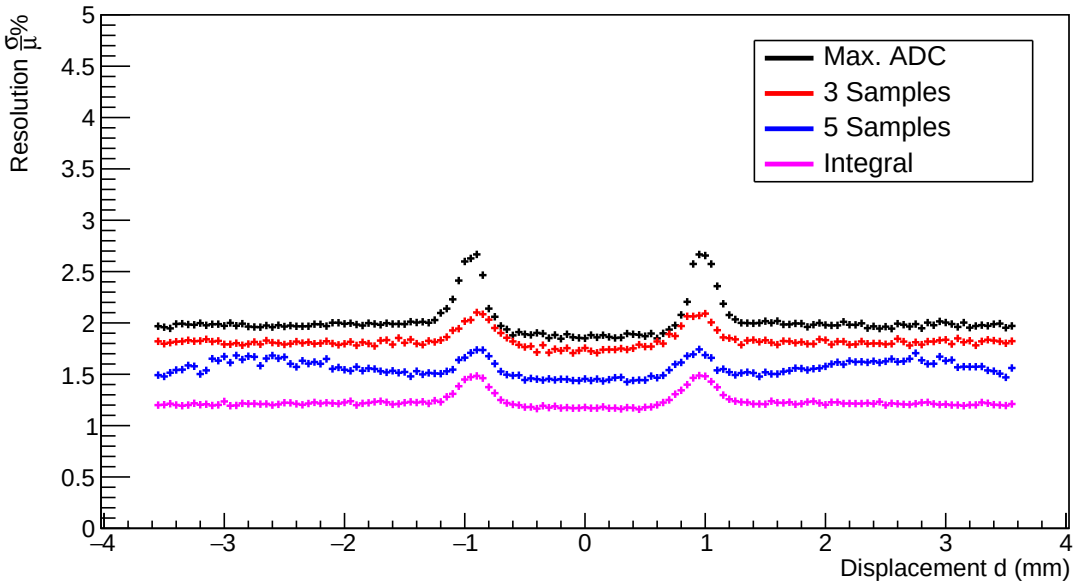

Figure 5.18: Resolution of cluster charge in dependence of displacement with SU2 = 3 ADC Units and a cluster charge of 200 ADC Units

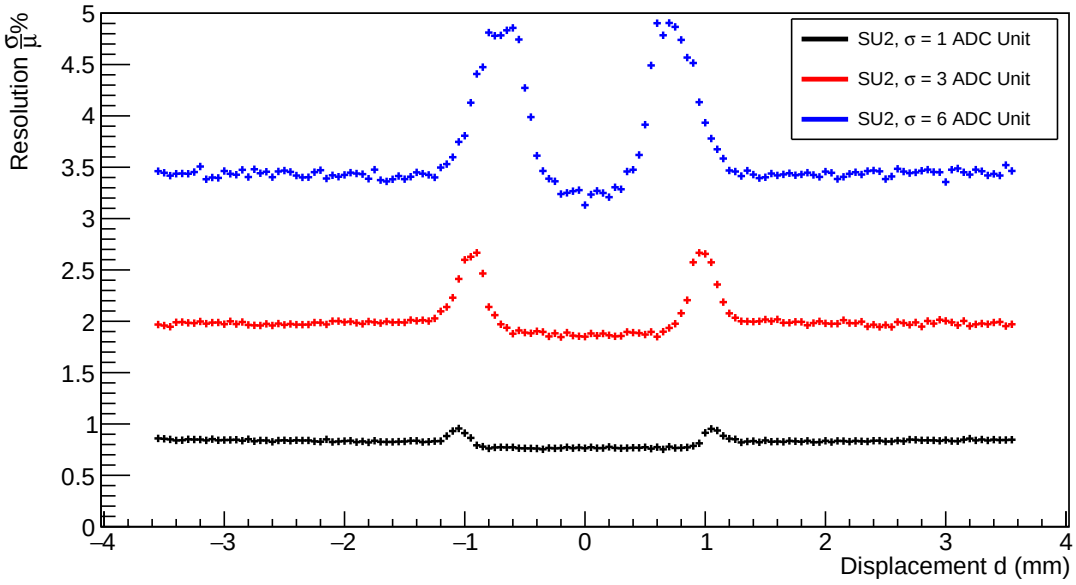

Figure 5.19: Resolution of cluster charge in dependence of displacement with SU2 at 1 ADC Unit, 3 ADC Units and 6 ADC Units and a cluster charge of 200 ADC Units using reconstruction method: Max. ADC.

The next expected uncertainty is SU2, and Figure 5.18 shows a clear distinction in the resolution for the methods, with Method 4 being the best at around 1.2% and Method 1 being the worst at around 2%. At around 0.6 mm, the fourth pad is triggered, leading to a deterioration of 0.3 percent points for Method 4 and 0.8 percent points for Method 1. After the methods have reached their plateau after around 1.3 mm, the resolution keeps being a bit worse than it was for a central hit. This is especially noticeably for Method 3, which suffers from the same effect it has for low cluster charges at a position near the border of two pads. Figure 5.19 shows the effect of increasing SU2 for Method 1. With increasing SU2 the displacement needed for more pads to trigger decreases from 1 mm to 0.2 mm for 1 ADC Units and 6 ADC Units respectively. Additionally the width and height of the effect increase, with a width of around 0.2 mm and height difference of around 0.2 percent points for 1 ADC Units to a width of around 1 mm and height difference of around 1.7 percent points for 6 ADC Units. The overall resolution deteriorates by about 2.6 percent points just by increasing the SU2 by 5 ADC Units, which is only 2.5% of the incoming cluster charge.

The effect of SU3 is displayed in Figures 5.20 and 5.21. Both show the effect on all methods with and without a pad restriction for a cluster charge of 200 ADC Units. In the range of 0.8 mm around the centre, Method 4 is clearly the best with a resolution of around 1.65%, while the other methods are around 2.3%. After a fourth pad is triggered, Method 1 and 2 are clearly affected the most and the resolution deteriorates to approximately 3.5%. Method 1 is not able to compensate the effect of SU3 and shows a rather strong fluctuation in the resolution. Even if Method 4 was better for hits close to the centre, after the fourth pad is triggered, the resolution diminishes to 2.6% and keeps getting worse for a more decentralised hit. On the other hand, Method 3 has a resolution for a central hit of around 2.2% and only deteriorates to 2.6%. At around 1.2 mm, Method 2 and 3 are better than Method 4 with Method 2 being slightly better than Method 3. When limiting the triggered pads to three, Method 4 is clearly the best option.

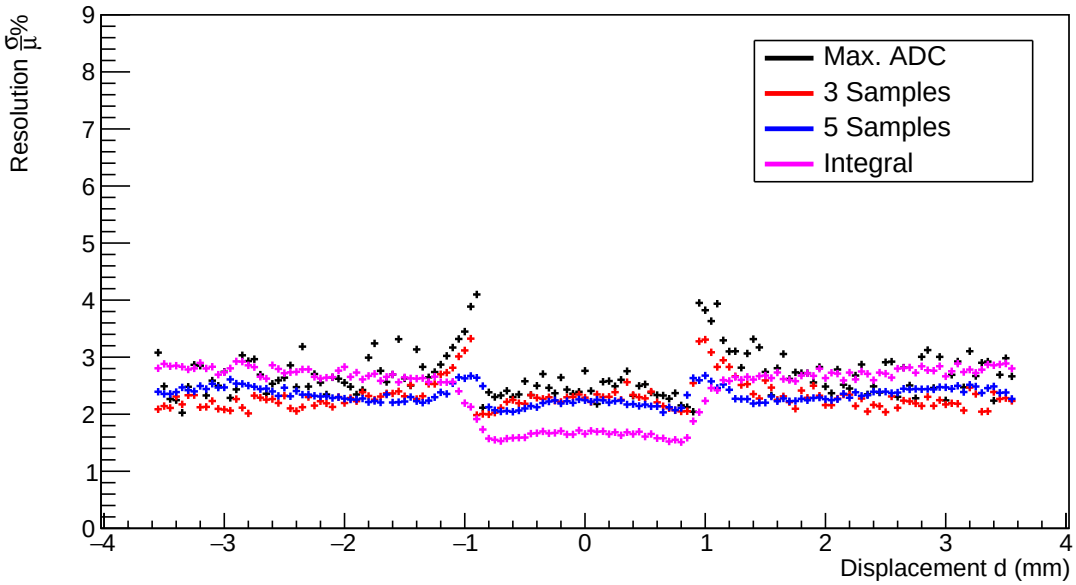

Figure 5.20: Resolution of cluster charge in dependence of displacement with SU3 with $A = 5$ ADC Units and a cluster charge of 200 ADC Units.

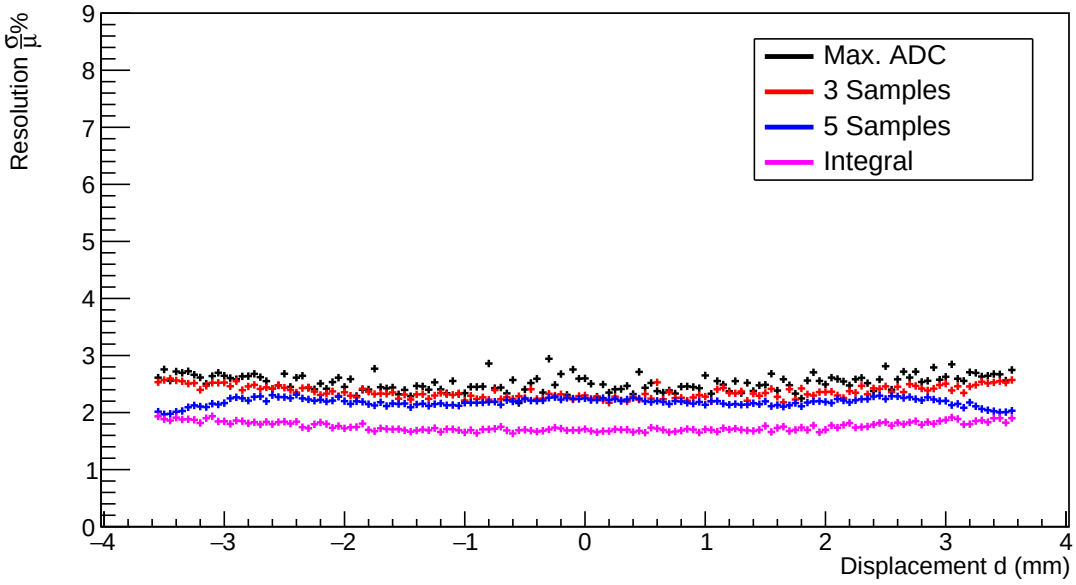

Figure 5.21: Resolution of cluster charge in dependence of displacement with SU3 with $A = 5$ ADC Units while limited to 3 Pads and a cluster charge of 200 ADC Units

Finally, all uncertainties are applied to the reconstruction methods and displayed in Figure 5.22 and Figure 5.23, which has the addition of a phase for the sampling steps of $\varphi = \pi$. Method 4 is now clearly separated from the other methods but has a slightly worse resolution at around 6.2% than with only SU1 and SU2 as seen in Figure 5.14. Additionally, the presence of SU3 shifts the displacement needed to trigger another pad, from 0.6 mm to 0.2 mm. The plateau reached by the differed method is also slightly higher than before. The addition of a phase to the sampling steps does not chance the overall course of the resolution or its magnitude to a noticeable degree.

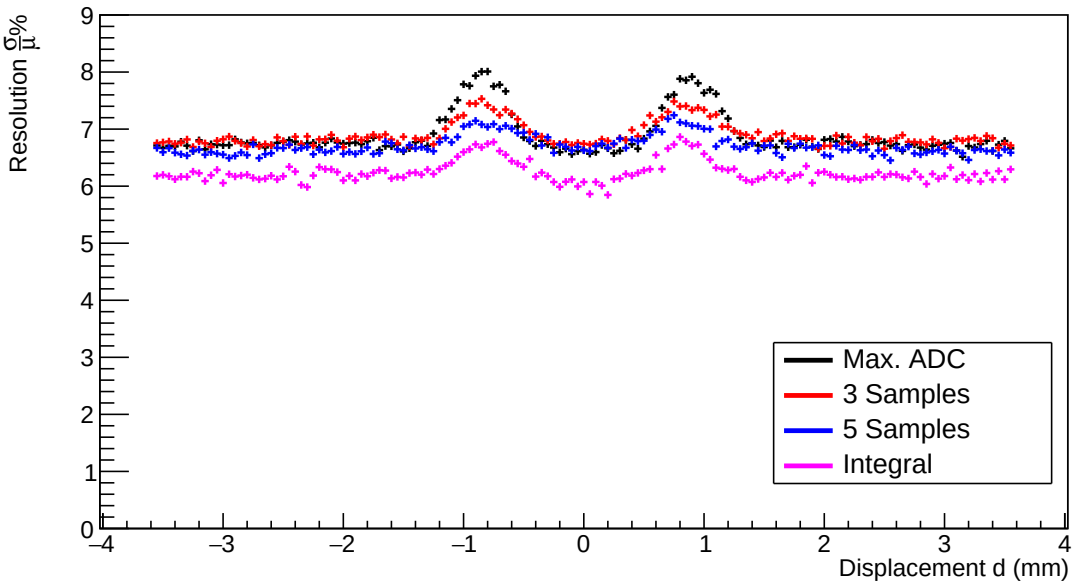

Figure 5.22: Resolution of cluster charge in dependence of displacement with SU1 = 6%, SU2 = 3 ADC Units, SU3 with A = 5 ADC Units and a cluster charge of 200 ADC Units.

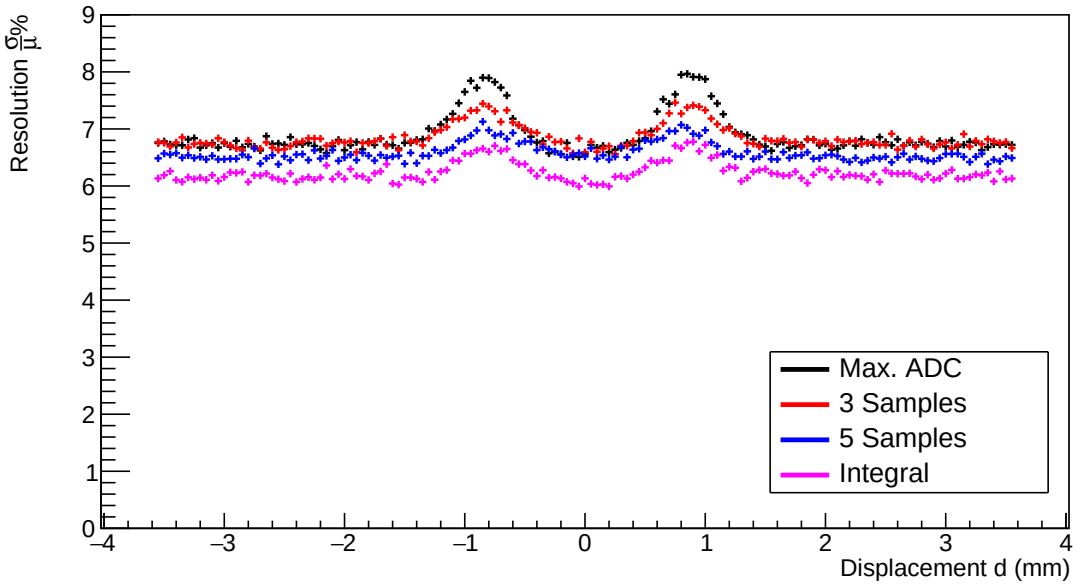

Figure 5.23: Resolution of cluster charge in dependence of displacement with SU1 = 6%, SU2 = 3 ADC Units, SU3 with $A = 5$ ADC Units, a pulse shape phase of $\varphi = \pi$, meaning that the pulse shape is sampled between the optimal sample positions and a cluster charge of 200 ADC Units.

5.2 Spatial Resolution

The position d of the displacement was calculated with the Centre-of-Gravity approach (equation 4.2). In the upcoming diagrams, the displacement difference Δd is the difference between the reconstructed positions d_{ideal}, which is the ideal hit reconstructed via Centre-of-Gravity with no signal uncertainties, and d_{SU}, the reconstructed hit with applied uncertainties. This means if $\Delta d > 0$ for $d_{ideal} > 0$ or $\Delta d < 0$ for $d_{ideal} < 0$ the reconstructed position d_{SU} is closer to the centre than the ideal position.

5.2.1 Variation of incoming Energy (A)

Figure 5.24 displays the displacement difference Δd for the variation of the cluster charge with SU1, SU2 and SU3 using Method 3. The hits were set to be at the centre of the pad and $\Delta d = 0$ for all simulated cluster charges. This behaviour is true for all variations of uncertainties and number of pads, as long as it is a central hit. The only thing that differs is the error bar, which decreases for higher cluster charges and increases after another pad is triggered.

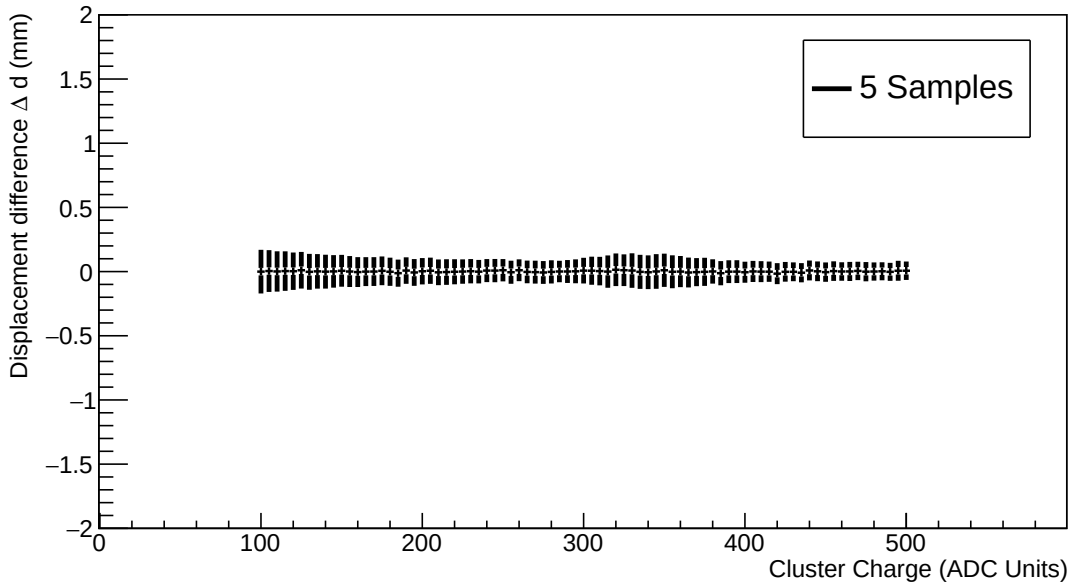

Figure 5.24: Displacement difference Δd dependence on cluster charge with SU1 = 6%, SU2 = 3 ADC Units and SU3 with A = 5 ADC Units. Reconstruction Method 3 (5 Samples) is shown.

5.2.2 Variation of Displacement (d)

In contrast to the variation of incoming energy, the variation of displacement is affected by the uncertainties. Since the behaviour is symmetrical, only the positive displacement will be discussed. Figure 5.25 displays the displacement difference, i.e., an additional shift of the reconstructed hit position with respect to the expected Centre-of-Gravity position, utilizing SU1 at 6% and SU2 with 3 ADC Units at a cluster charge of 200 ADC Units for all methods. In the region close to the centre, until 0.8 mm, the difference becomes slightly larger to 0.08 mm for Method 1, which means that the reconstructed position is closer to the centre. After the fourth pad is triggered, Δd declines to -0.3 mm and the absolute value of the difference becomes smaller by increasing the displacement d.

This effect can be seen by all methods and gets smaller for Method 2 and 3, but increases for Method 4 with -0.15 mm, -0.11 mm and -0.17 mm respectively. Figure 5.26 shows the same configuration with a limitation to three pads. The overall effect of the uncertainties is that Δd increases for an increasing displacement. Method 1 has the highest difference of 0.27 mm for a hit directly between two pads, while Method 3 is the best option in that case with only 0.05 mm of difference.

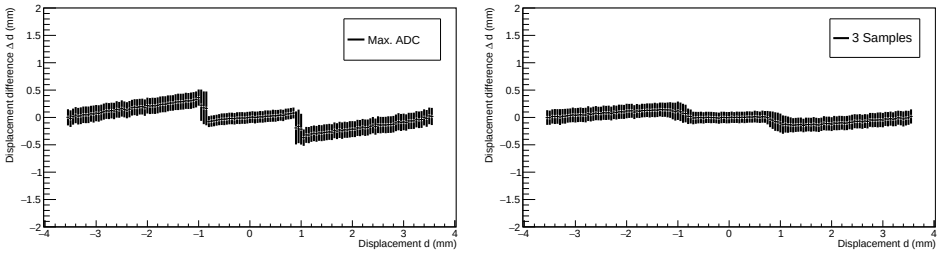

(a) Method 1 (Max. ADC) **(b)** Method 2 (3 Samples)

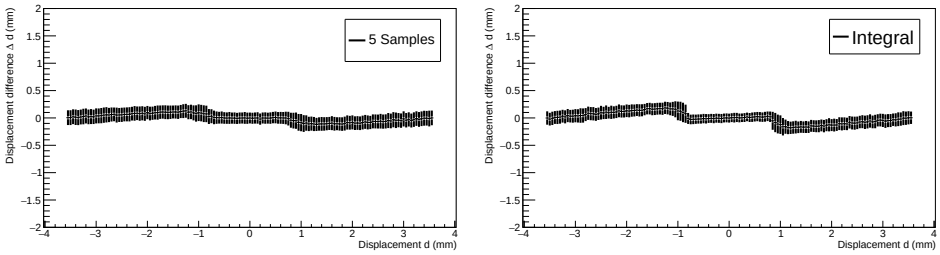

(c) Method 3 (5 Samples) **(d)** Method 4 (Integral)

Figure 5.25: Displacement difference Δd dependence on displacement d with SU1 = 6%, SU2 = 3 ADC Units and a cluster charge of 200 ADC Units.

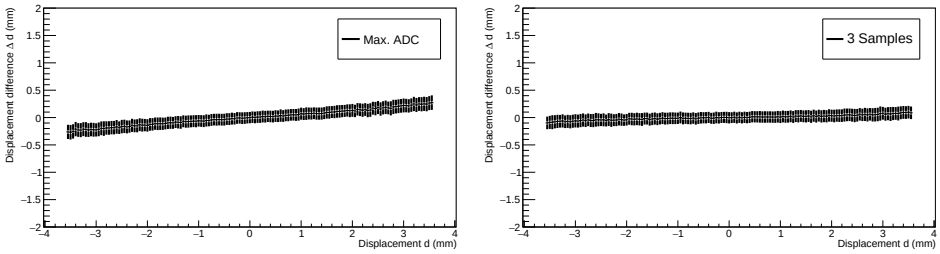

(a) Method 1 (Max. ADC) **(b)** Method 2 (3 Samples)

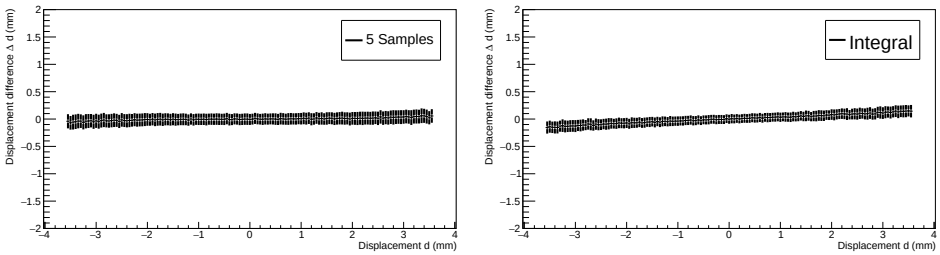

(c) Method 3 (5 Samples) **(d)** Method 4 (Integral)

Figure 5.26: Displacement difference Δd dependence on displacement d with SU1 = 6%, SU2 = 3 ADC Units while limited to 3 Pads and a cluster charge of 200 ADC Units.

Figure 5.27 displays the same uncertainties on a cluster charge of 330 ADC Units. With this cluster charge, already five pads are triggered leading to an immediate difference of $-0.25\,\text{mm}$ for Method 1. After this, the diagrams show the typical behaviour of increasing Δd as displayed in Figure 5.26. Again, Method 3 is the best option with the smallest effect due to the triggered pads of around 0.08 mm and an overall small difference.
Figure 5.28 shows the the effect of SU1 for all methods at a cluster charge of 200 ADC Units. As expected, the difference is close to zero, while some fluctuations at the border of two pads can be observed with higher error bars.

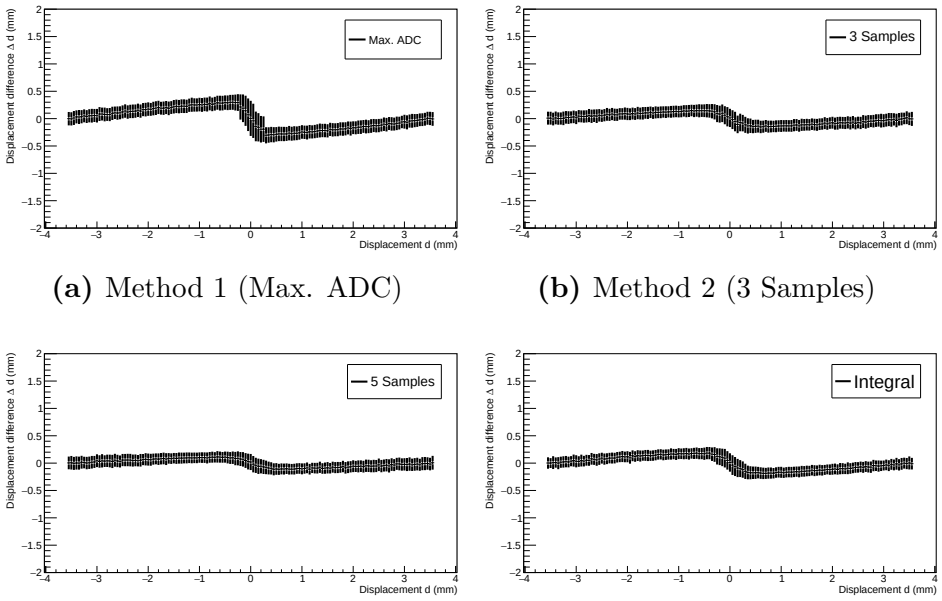

(a) Method 1 (Max. ADC) **(b)** Method 2 (3 Samples)

(c) Method 3 (5 Samples) **(d)** Method 4 (Integral)

Figure 5.27: Displacement difference Δd dependence on displacement d with SU1 = 6%, SU2 = 3 ADC Units and a cluster charge of 330 ADC Units.

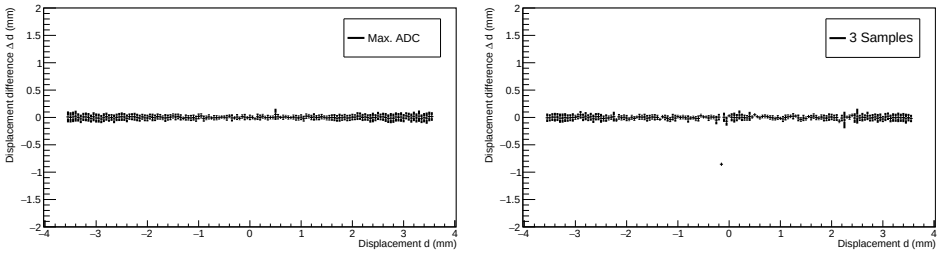

(a) Method 1 (Max. ADC) **(b)** Method 2 (3 Samples)

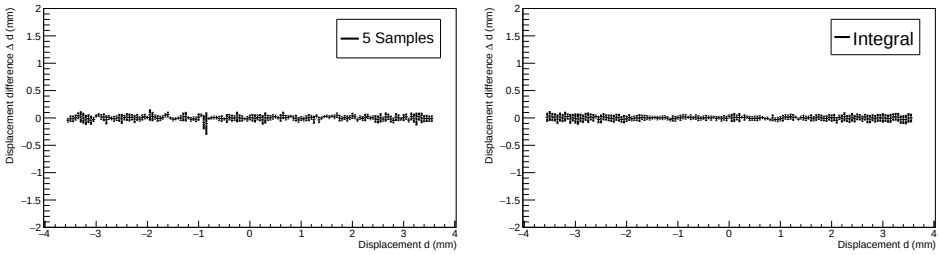

(c) Method 3 (5 Samples) **(d)** Method 4 (Integral)

Figure 5.28: Displacement difference Δd dependence on displacement d with SU1 = 6% a cluster charge of 200 ADC Units.

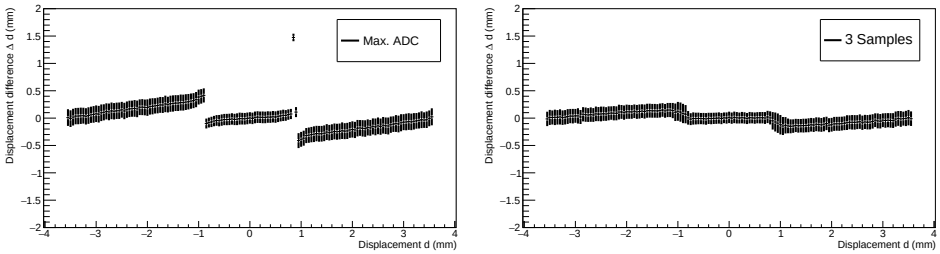

(a) Method 1 (Max. ADC) **(b)** Method 2 (3 Samples)

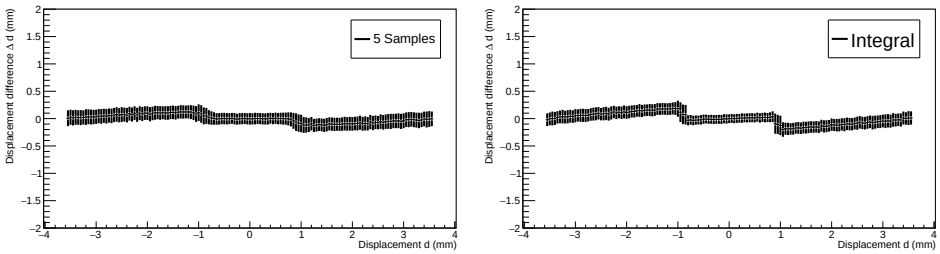

(c) Method 3 (5 Samples) **(d)** Method 4 (Integral)

Figure 5.29: Displacement difference Δd dependence on displacement d with SU2 = 3 ADC Units and a cluster charge of 200 ADC Units.

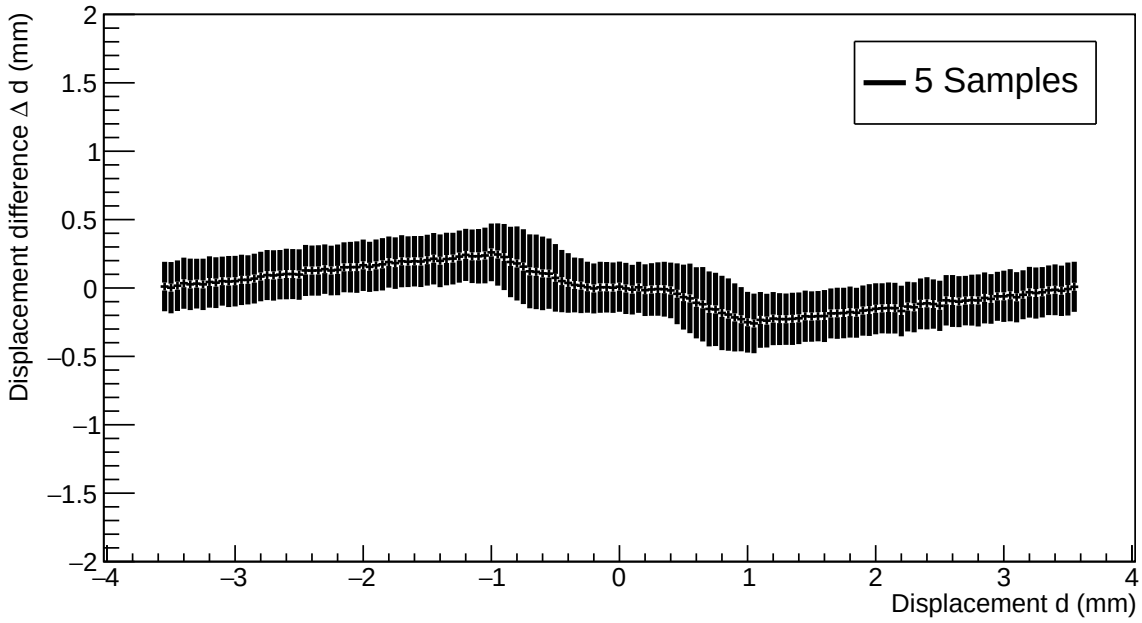

Figure 5.30: Displacement difference Δd dependence on displacement d with SU2 = 6 ADC Units and a cluster charge of 200 ADC Units for Method 3 (5 Samples).

Taking a deeper look into the effects of the different uncertainties, Figure 5.29 displays the influence of SU2 with 3 ADC Units for the different methods. Method 1 displays the highest difference after around 1.1 mm with approximately -0.41 mm. The other methods are better at compensating SU2 with Method 3 being the most accurate, having only a slightly deterioration of -0.11 mm. While all methods reach a difference of zero after increasing the displacement, Method 3 does it in a shorter distance. Since Method 3 is the best option for SU2, Figure 5.30 displays Method 3 with an uncertainty of 6 ADC Units. The first prominent difference is the change in displacement when the fourth pad is triggered. It shifts from 1.1 mm to 0.3 mm and deteriorates the displacement difference to -0.23 mm and more than doubles it compared to Figure 5.29. Additionally the displacement needed to reach a dislocation of around zero again increases as well.

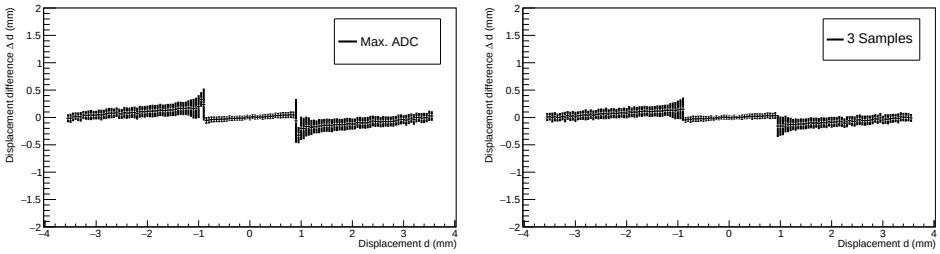

(a) Method 1 (Max. ADC) **(b)** Method 2 (3 Samples)

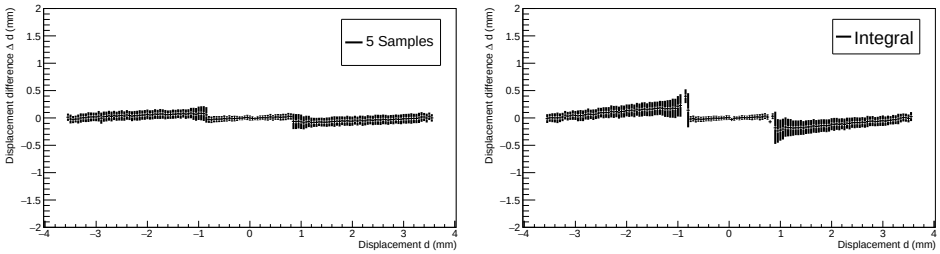

(c) Method 3 (5 Samples) **(d)** Method 4 (Integral)

Figure 5.31: Displacement difference Δd dependence on displacement d with SU3 with $A = 5\,\text{ADC Units}$ and a cluster charge of 200 ADC Units.

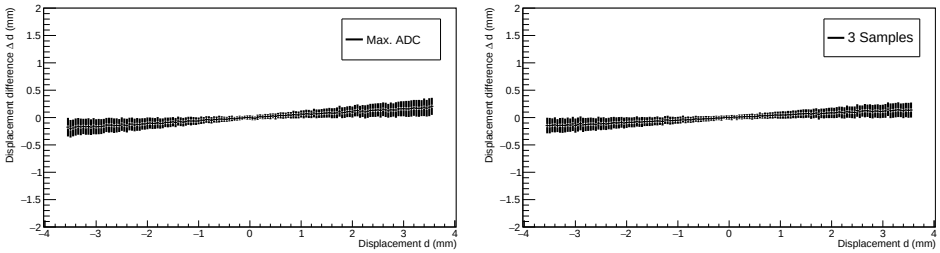

(a) Method 1 (Max. ADC) **(b)** Method 2 (3 Samples)

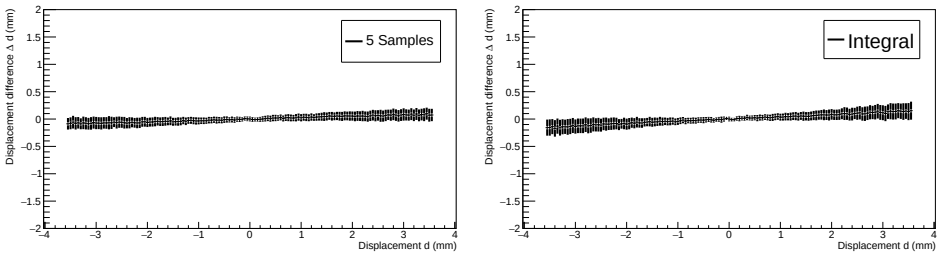

(c) Method 3 (5 Samples) **(d)** Method 4 (Integral)

Figure 5.32: Displacement difference Δd dependence on displacement d with SU3 with $A = 5\,\text{ADC Units}$ while limited to 3 Pads and a cluster charge of 200 ADC Units.

The influence of SU3 is displayed in Figures 5.31 and 5.32, with a limitation to three pads. This uncertainty is prominent at Method 1 and 4 with a maximum difference of $-0.2\,\text{mm}$ and $-0.22\,\text{mm}$, respectively. The high error bars around the critical point for the fourth pad imply that the displacement difference could be much higher by using these methods. Method 3 shows only a difference of about $-0.09\,\text{mm}$. Without the fourth pad, the pure effect of the uncertainty can be seen in Figure 5.32 and shows that Method 3 has a difference of $0.07\,\text{mm}$ compared to Method 4 with $0.15\,\text{mm}$ as well as being more stable than Method 4.
Lastly, all three uncertainties are added together and the result is displayed in Figures 5.33 and 5.34 with an additional pulse shape phase of $\varphi = \pi$. As expected, both variations show a worse result for the displacement difference than Figure 5.25, which only had SU1 and SU2 applied. Among themselves, the addition of a phase worsens Δd in an negligible amount. Method 3 still remains the most optimal reconstruction method for the task and has the highest difference of only $-0.17\,\text{mm}$ compared to its highest difference with only two uncertainties applied of $-0.11\,\text{mm}$. On the other hand, Method 4 has a maximum difference of $-0.28\,\text{mm}$ and $-0.17\,\text{mm}$ for only two applied uncertainties, demonstrating that it is more influenced by SU3 than Method 3. Method 1 and 2 deteriorate to $-0.55\,\text{mm}$ and $-0.22\,\text{mm}$ with the first method being the one that is affected the most by the addition of SU3.

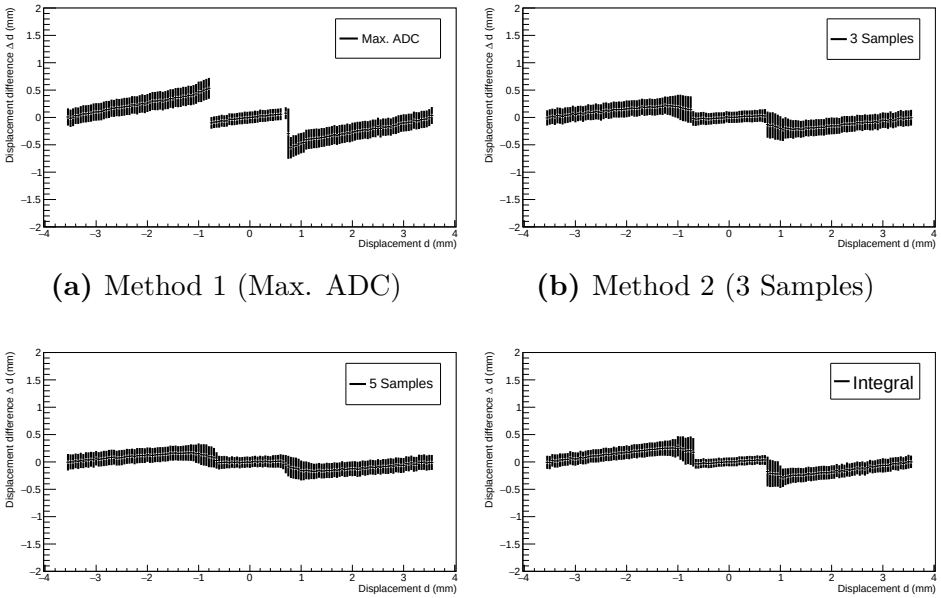

(a) Method 1 (Max. ADC) **(b)** Method 2 (3 Samples)

(c) Method 3 (5 Samples) **(d)** Method 4 (Integral)

Figure 5.33: Displacement difference Δd dependence on displacement d with SU1 = 6%, SU2 = 3 ADC Units, SU3 with $A = 5$ ADC Units and a cluster charge of 200 ADC Units.

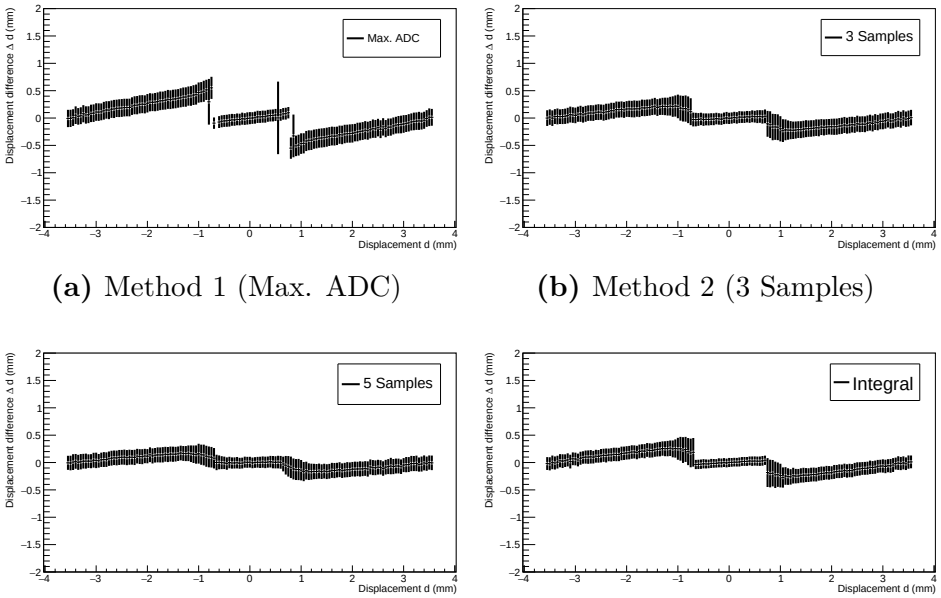

(a) Method 1 (Max. ADC) **(b)** Method 2 (3 Samples)

(c) Method 3 (5 Samples) **(d)** Method 4 (Integral)

Figure 5.34: Displacement difference Δd dependence on displacement d with SU1 = 6%, SU2 = 3 ADC Units and SU3 with $A = 5$ ADC Units, a pulse shape phase of $\varphi = \pi$, meaning that the pulse shape is sampled between the optimal sample positions, and a cluster charge of 200 ADC Units.

5.2.3 Fluctuation width of position reconstruction

The fluctuation level of the reconstructed positions is described by the width σ of the Gaussian distribution and therefore a measure for the resolution of the spatial reconstruction method. In the previously shown diagrams the error bar displayed was 1σ of the Gaussian distributed position. Since Figure 5.33 shows the shift of the spatial reconstruction due to the three applied signal uncertainties, Figure 5.35 shows the width σ. The worsening of the resolution around the critical positions mentioned before can be seen, but a mostly constant plateau around the centre and between two pads with $\sigma = 0.1\,\text{mm}$ and $\sigma = 0.14\,\text{mm}$, respectively, demonstrates the overall spatial resolution. At around $d = 0.9\,\text{mm}$, the resolution gets to $\sigma = 0.2\,\text{mm}$, but as mentioned before this effect can be suppressed by ignoring more than three pads.

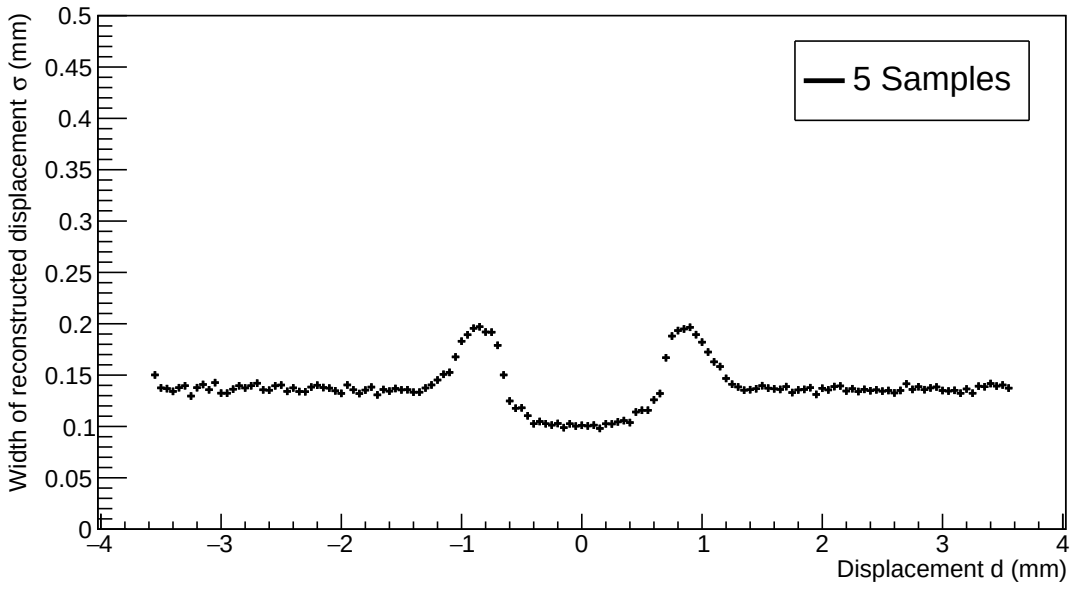

Figure 5.35: Width of reconstructed displacement σ dependence on displacement d with SU1 = 6%, SU2 = 3 ADC Units and SU3 with $A = 5$ ADC Units and a cluster charge of 200 ADC Units for Method 3.

5.3 Peaking Time

Simulations so far were using a peaking time of $\tau = 240\,\text{ns}$, i.e., the parameter of the analogue front-end in SPADIC 2.0. Here the system behaviour with the newly chosen (SPADIC 2.2) peaking time $\tau = 120\,\text{ns}$ is investigated. Figure 5.36 displays the resolution dependent on the cluster charge with the same uncertainty settings as Figure 5.1, while using a peaking time of $\tau = 120\,\text{ns}$. The behaviour around low cluster charges is now much more equal for Method 1 to 3, but still around 7%, while Method 4 is the best around 6.3%. A significant difference is the course of the resolution after more pads are triggered. Before, Method 1 was clearly the worst option and it still is, but the difference to the other methods is much smaller and in the region of 330 ADC Units to 400 ADC Units, Method 3 is slightly better than Method 4 with a peaking resolution of 6.36% and 6.58%, respectively. Furthermore, the critical region became bigger from 260 ADC Units to around 420 ADC Units eventually reaching a plateau.

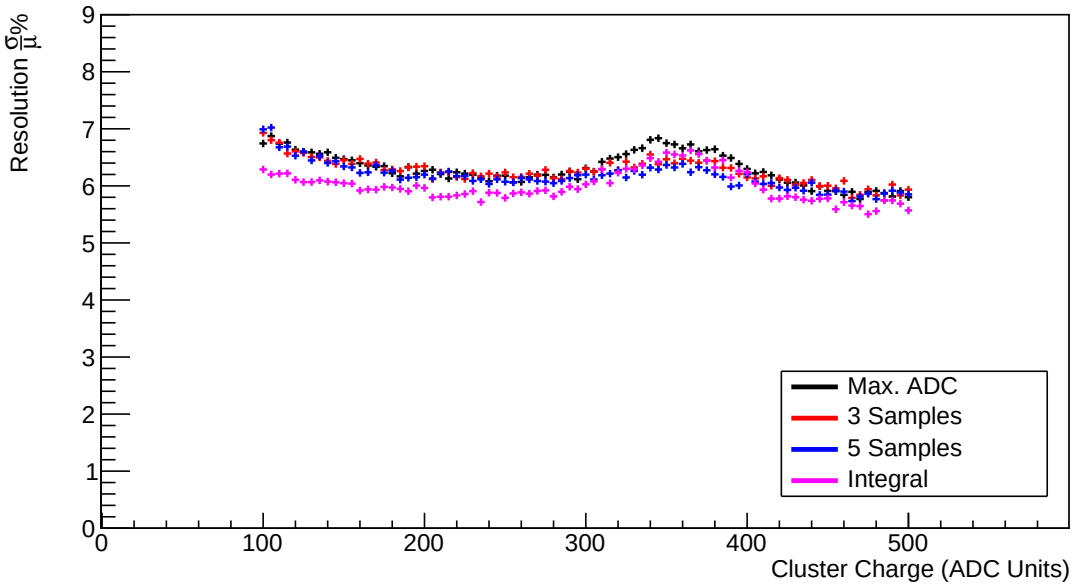

Figure 5.36: Resolution of cluster charge in dependence of cluster charge with SU1 = 6%, SU2 = 3 ADC Units and a peaking time of $\tau = 120\,\text{ns}$.

6 Summary

The simulation framework which was designed, created and employed for this thesis was used to investigate effects of the signal characteristics on the overall system resolution. Different signal extraction methods have been compared concerning the effective energy and spatial resolution. The framework itself offers a multitude of changeable variables and probes along the signal path on the inspected hit sample. One of the main features of the framework is the ability to look at the effect of single signal uncertainties with and without the effect of other signal uncertainties and to make a prediction about how the resolution could change.
In chapter 5.1 a deeper look into the energy resolution was taken and it was possible to show that all methods were equally reliable when only a general finite resolution of the MWPC was modelled (SU1). The method to sum over all simulated 32 samples (Method 4) became the preferred method for most applications due to its stability and low sensitivity to the simulated signal uncertainties. The only exception was found for additionally assumed oscillating signal distortions SU3 at high cluster charges, where the 32-sample summing was outdone by evaluating only five samples centred around the maximum position (Method 3), not only by the overall deterioration of 0.35 percent points from 1.74% to 2.09% for Method 3 compared to 0.8 percent points from 1.23% to 2.03% for Method 4. The best resolution at high cluster charges was achieved by Method 3 with 1.46% and was better than Method 4 with a resolution of only 1.7%. Nevertheless, it is noted that the transport of 32 samples exceeds the data rate capabilities of the final experiment, being operated at high interaction rates and is, therefore, to be understood as a reference method in this context. Since all methods are almost equal in the high cluster charge region, Method 3 could be the better choice if SU3 would appear even larger than simulated in this thesis. It was shown that the choice of the signal extraction is of higher importance, the larger the channel-individual signal fluctuations (SU2) and oscillating changes (SU3) are assumed relative to the common MWPC resolution (SU1). Another point the framework made clear is the severe effect

of SU2, showing that already small changes have a great impact. As seen in Figure 5.9, additional overall fluctuation from this simulation degrade the overall resolution, as already accounted for the MWPC itself.
Furthermore, effects on the spatial resolution (chapter 5.2) were put under scrutiny. In contrast to the energy resolution, the Center-of Gravity approach (4.2) was used to calculate the displacement d with the idealized and uncertain samples. Method 3 was shown to be the preferable method in all simulation settings. Due to the characteristics of the Centre-of-Gravity approach, signal uncertainties were shown to impose position-dependent shifts of the reconstructed position to one or the other direction. With all three uncertainties applied, those shifts were found to be about $\Delta d = 0.13\,\mathrm{mm}$ top, which is significant compared to the detector design spatial resolution of about 0.3 mm (Gaussian width) [TDR18]. On the other hand, sing only the maximum sample for charge extraction (Method 1), even a difference of about $\Delta d = 0.35\,\mathrm{mm}$ as shown in Figure 5.26, was found.
However, the most prominent reason for a deterioration in the resolution that showed up during the simulation, was the effect of triggering more pads and including them in the analysis. In all cases, a fourth or fifth pad made the resolution worse until the corresponding pads would detect high enough fractions of the cluster charge to give more actual data into the reconstruction method than uncertainties. Derived can be the recommendation to restrict the analysis to the evaluation of three neighboured channels independent of the triggered cluster size. Constraints in the real experiment may arise from energy depositions of protons and/or heavy nuclei, which has to be scrutinised in detail. Another point is the design of the reconstruction methods itself. Since the reconstruction would always determine the maximum sample, adding three (Method 2) or five samples (Method 3) would lead to worse results, as soon as the uncertainties would cause a sample far off the idealized sample to be taken. This effect was in particular visible for Method 3 at a low cluster charges (compare Figure 5.1).
Chapter 5.3 briefly showed the effect of a shorter peaking time and even if the differences seemed small it could be interesting to look at a deeper analysis with the current SPADIC value.
Overall, the framework was able to fulfil its purpose to disentangle the impact of particular signal uncertainties and fluctuations on the extracted charge and position values. It can still be expanded and worked upon to make it simpler and more convenient to use, while the current reconstruction method can easily be replaced to analyse other

methods or compare new methods to already existing ones. Also, the consideration of further signal characteristics is easily possible. Another interesting aspect could also be the integration of time resolution. The next decisive step of application of this simulation framework is the comparison of the simulated performances to real data. The full simulation framework is made available in a *git* project in the common TRD group project space.

Abbreviations

ADC Analog-to-Digital Converter

ASIC Application Specific Integrated Circuit

CBM *Compressed Baryonic Matter*

CRI Common Readout Interface

CSA Charge Sensitive Amplifier

DSP Digital Signal Processor

FAIR Facility for Antiproton and Ion Research

FEB Front-End Board

FLES First Level Event Selector

FLIB FLES Interface Board

FPGA Field Programmable Gate Array

GSI *GSI Helmholtzzentrum für Schwerionenforschung*

IC Integrated Circuit

MAPS Monolithic Active Pixel Sensor

MUCH Muon Chamber System

MVD Micro-Vertex Detector

MWPC Multi Wire Proportional Chamber

PRF Pad Response Function

PSD Projectile Spectator Detector

QCD *Quantum Chromodynamics*

QGP Quark Gluon Plasma

RICH Ring Imaging Cherenkov Detector

ROB Read-Out Board

SPADIC Self-triggered Pulse Amplification and Digitisation as IC

STS Silicon Tracking System

SU Simulated Uncertainty

TOF Time-of-Flight System

TR Transition Radiation

TRD Transition Radiation Detector

Bibliography

[Rol08] Walter Blum, Werner Riegler, Luigi Rolandi. *Particle Detection with Drift Chambers*. 2nd ed. Springer Berlin, Heidelberg, 2008. ISBN: 978-3-540-76683-4. URL: https://doi.org/10.1007/978-3-540-76684-1.

[AW12] A. Andronic and J.P. Wessels. "Transition radiation detectors". In: *Nuclear Instruments and Methods in Physics Research Section A: Accelerators, Spectrometers, Detectors and Associated Equipment* 666 (Feb. 2012), pp. 130–147. DOI: 10.1016/j.nima.2011.09.041. URL: https://doi.org/10.1016%2Fj.nima.2011.09.041.

[Arm13] T. Armbruster. "SPADIC – a Self-Triggered Detector Readout ASIC Wirth Multi-Channel Amplification and Digitization." Dissertation. 2013.

[Ber14] Cyrano S.H. Bergmann. "Development, Simulation and Test of Transition Radiation Detector Prototypes for the Compressed Baryonic Matter Experiment at the Facility for Antiproton and Ion Research". Dissertation. 2014.

[Sau14] Fabio Sauli. *Gaseous Radiation Detectors: Fundamentals and Applications*. Cambridge University Press, 2014. ISBN: 978-1-107-04301-5.

[Her16] Norbert Wermes Hermann Kolanoski. *Teilchendetektoren. Grundlagen und Anwendungen*. 1st ed. Springer Spektrum Berlin, Heidelberg, 2016. ISBN: 978-3-662-45349-0. URL: https://doi.org/10.1007/978-3-662-45350-6.

[TDR18] *The Transition Radiation Detector of the CBM Experiment at FAIR : Technical Design Report for the CBM Transition Radiation Detector (TRD)*. Tech. rep. FAIR Technical Design Report. Darmstadt, 2018.

[Tan+18] M. Tanabashi et al. "Review of Particle Physics". In: *Phys. Rev. D* 98 (3 Aug. 2018), p. 030001. DOI: 10.1103/PhysRevD.98.030001. URL: https://link.aps.org/doi/10.1103/PhysRevD.98.030001.

[Käh20] Phlipp Kähler. "Private communitcation and internal report". Sept. 2020.

[Her] Norbert Hermann. *38th CBM Collaboration Meeting*. URL: https://indico.gsi.de/event/13089/contributions/55842/attachments/37147/49690/Opening_nh.pdf. accessed: 12.02.2023.

Acknowledgements

I would like to thank Prof. Dr. Andronic and Prof. Dr. Klein-Bösing for the opportunity to work on this thesis and the provided help and support throughout the duration of the working period. Special thanks go to Philipp Kähler, who supervised my work and supported me with helpful discussions, explanations and consultations even during the home office time due to the corona pandemic and also to Philipp Munkes, who helped me with all programming related questions. Finally I would like to thank my parents Sylvia and Arnim Morgenweck, it would not have been possible without their support over the years.

Eigenständigkeitserklärung

Hiermit versichere ich, dass die vorliegende Arbeit über *A Signal Simulation Framework for the CBM-TRD FEE* selbstständig von mir und ohne fremde Hilfe verfasst worden ist, dass keine anderen Quellen und Hilfsmittel als die angegebenen benutzt worden sind und dass die Stellen der Arbeit, die anderen Werken – auch elektronischen Medien – dem Wortlaut oder Sinn nach entnommen wurden, auf jeden Fall unter Angabe der Quelle als Entlehnung kenntlich gemacht worden sind. Mir ist bekannt, dass es sich bei einem Plagiat um eine Täuschung handelt, die gemäß der Prüfungsordnung sanktioniert werden kann.

Ich erkläre mich mit einem Abgleich der Arbeit mit anderen Texten zwecks Auffindung von Übereinstimmungen sowie mit einer zu diesem Zweck vorzunehmenden Speicherung der Arbeit in einer Datenbank einverstanden.

Ich versichere, dass ich die vorliegende Arbeit oder Teile daraus nicht anderweitig als Prüfungsarbeit eingereicht habe.

(Datum, Unterschrift)